Nanotextured Mold Surface with DLC coating for Reduction in Residual Ceramic Particles

Motoyuki Murashima[1*], Koki Hojo[1], Shigehiro Ito[1], Noritsugu Umehara[1], Takayuki Tokoroyama[1], Tomonori Takahashi[2], Minoru Imaeda[2]

[1] Department of Micro-Nano Mechanical Science and Engineering, Nagoya University

Furo-cho, Chikusa-ku, Nagoya city, Aichi 464-8603, Japan

[2] NGK Insulators, Ltd.

2-56, Suda-cho, Mizuho-ku, Nagoya city, Aichi 467-8530, Japan

Email address of corresponding author: motoyuki.murashima@mae.nagoya-u.ac.jp

Abstract

In the ceramic industry, ceramic particles remaining on the mold surface require surface cleaning during press molding, reducing productivity. Surface texturing and ta-C (tetrahedral amorphous carbon) coatings are well-known surface-energy controllable treatments developed for low adhesion, low friction and high wear resistance. In the present paper, we demonstrate the effect of reducing ceramic residues using nanotexturing, ta-C coatings, and their combination. We compared two surface morphologies (i.e., 770-nm pitch nanotexturing and flat) and five materials (i.e., non-hardened steel, hardened steel, ta-C and two types of ta-CNx (nitrogen doped ta-C)). Molding test results show that the ta-C coating on flat surfaces with the highest hardness of 30 GPa shows the lowest residual amount of 5.9 μg for Al_2O_3 ceramic particles. The amount is 82 % less than the non-hardened steel. The ta-CNx_{20}, made with a nitrogen flow rate of 20 sccm, shows the lowest residual amount of 234 μg for SiO_2 ceramic particles, which is 81 % less than the non-textured ta-CNx_{20}. In conclusion, we provide design guidelines for nanotextured mold surface; the texturing pitch should be small enough for ceramic particles; the mold surface should sufficiently hard; the lower the surface energy per unit area, the less residues of ceramic particles.

Keyword: nanotexture; ta-C and ta-CNx coatings; ceramic particle residue; press molding; mold surface

1. Introduction

Powder formation is a very important technology in a wide range of industrial fields (e.g., ceramic, pharmaceutical, chemical, food, and mineral industries).[1-13] Especially in the ceramic industry, power handling technology is important because of the demand for high-quality and high-precision products. Many ceramic applications are formed using a press molding processes.[14-15] In the process, residues remain on the mold surface, resulting in an increase in surface roughness, dimensional deterioration, and poor functionalities. In addition, the mold needs to be cleaned frequently to remove the residues, reducing productivity. Therefore, there is

a strong need for new techniques to reduce ceramic residues.

Many types of adhesive forces affect the micro/nanoscale particle. Most of them are developed from surface energy (i.e., van der Waals force and electrostatic interactions), electrostatic force, and meniscus force due to water molecules in the atmosphere.[16-19] Although several active-control methods of adhesion and friction was proposed,[20-27] surface treatment is still a reliable method and widely used in industrial fields. The surface treatment methods included surface texturing and coatings for controlling surface energy.

Today, many unique surface morphologies that mimic skin of plants and animals are developed to realize new functionalities. The emulation of the nature systems is called biomimetics. One of the most successful biomimetics surfaces is derived from lotus leaves.[28-32] It is well known that lotus leaves maintain clean surfaces even in dirt soil, due to many microscale protrusions covered with wax. Generally, surface texturing enhances its surface properties by increasing the ratio of surface area to volume.[31,32] For lotus leaves, the combination of the hydrophobic wax and micro protrusions provides such superhydrophobicity. Water droplets on the superhydrophobic surface remove dust and small particles, resulting in a self-cleaning surface.

Surface texturing is one of the key technologies for realizing new functional surfaces.[33-38] Therefore, many researchers and engineers challenged to create lotus-leaf-like surface structures using MEMS (micro-electro-mechanical systems), laser processing and additive manufacturing technologies.[39-43] The artificially created surfaces provide superhydrophobicity, low surface energy, and low hydrodynamic resistance,[31,44] giving industrially beneficial properties (e.g., low adhesion, low friction, and self-cleaning)[37,38,45-49]. Recently, nanoscale texturing is created using a femtosecond laser. The femtosecond laser is able to produce LIPSS (laser-induced periodic surface structure) by laser interference between the irradiated laser and reflected laser from surface roughness.[50-53] The super-short irradiation period and high-peak power of the femtosecond laser reduce the thermal damage to the textured surfaces.[53,54]

Coating technology is widely used in engineering application to provide functional surfaces. Coatings provide superior surface properties due to high-performance materials, while reducing the cost of the application by using inexpensive substrates. In recent year, DLC (diamond-like carbon) coatings attract attention as new carbonaceous hard coatings due to their high hardness, chemical inertness, and low friction properties.[55-60] Moreover, many characteristics (e.g., surface energy, friction properties, and oiliness) can be controlled by doping with other elements (e.g., nitrogen, silicon, boron, and fluorine).[61-74] Therefore, the DLC coatings already have many industrial applications (e.g., mold, piston ring, and drill).[75-87] Recently, it is revealed that a type of hard DLC coatings, ta-C (tetrahedral amorphous carbon), and ta-CNx (nitrogen doped ta-C) have excellent thermal stability and high wear resistance due to a high fraction of carbon sp^3 orbital bonding.[88-99] Therefore, these coatings are considered next-generation

functional coatings.

In the present paper, we show that the combination of the nanotexturing and ta-C coatings reveals excellent properties for reducing the amount of ceramic residue on the mold surface. In molding tests, alumina (Al_2O_3) and silica (SiO_2) particles are used as representative ceramic particles. The results demonstrate the importance of coating hardness, texturing pitch and surface energy for reducing ceramic residues.

2. Experiment Method

2.1. Nanotexturing, ta-C Coating, and ta-CNx Coatings

We used an ion-beam-assisted filtered arc-deposition method (IBA-FAD) to deposit ta-C and ta-CNx coatings. The IBA-FAD system achieves simultaneous deposition of carbon ions by the FAD method and nitrogen ions by an ion gun. It is well known that the deposition using arc discharge produces highly ionized carbon atoms, resulting in a homogeneous and hard carbonaceous coating.[100-102] However, the arc discharge also produces micro/nanoscale carbon clusters, which eventually grow into droplets in/on the coating. Because the droplets cause high wear and degradation of the coating,[103-108] lapping and polishing are usually used to remove the droplets.[108,109] However, theses method cannot completely remove the droplets. Therefore, droplet-filtering methods during arc deposition was developed.[100-102] The FAD method uses an electromagnetic field to separate ionized carbon atoms from non-ionized carbon clusters. The electromagnetic field generated by coils bends the ionized carbon beams and guides them to the substrate. On the other hand, the non-ionized carbon clusters pass straight through and are captured by a collecting film. The T-shape-filtering system of our coating equipment (VACS-110H, ONWARD GIKEN CO.LTD, Japan) efficiently collects the carbon clusters, resulting in a hard and droplet free ta-C coating.[110-112]

Doped atoms into a DLC coating provide the coating with a variety of properties (e.g., surface energy, amount of dangling-bond, friction property and wear properties). The nitrogen doped DLC, called CNx (carbon nitride), shows excellent tribological properties.[65-70] Moreover, the ta-CNx coatings have high hardness and less dangling-bonds, resulting in low friction and chemical affinity.[97-99] The present paper also demonstrates the performance of the ta-CNx coatings for reducing the residues of the ceramic particles. The nitrogen ion beams generated from the ion gun was irradiated from a direction tilted 90 degrees from the carbon ion beams. A rotation stage on which substrates were mounted rotated during the deposition process, realizing dynamic-mixing deposition of carbon and nitrogen atoms (Figure S1).

Prior to the deposition process, argon sputter cleaning was conducted for 15 minutes using the ion gun with an argon flow rate of 8 sccm and discharge voltage of 1.5 kV. The back pressure in the vacuum chamber was 4.0×10^{-3} Pa. Subsequently, arc discharge from a trigger

produced highly ionized carbon ions from a carbon target. The target with a diameter of 50 mm had a carbon purity of over 99.00 %. The arcing conditions were a current of 50 A and substrate bias of -100 V. The negative substrate bias accelerated carbon ions, resulting in a high-density coating. The deposition time and stage rotation speed were 40 minutes and 10 rpm, respectively. The ion gun was operated with a discharge voltage of 1 kV. The nitrogen flow rate varied from 0 to 20 sccm to deposit a variety of ta-C/ta-CNx coatings. In the present paper, the ta-C/ta-CNx coatings with nitrogen flow rates of 0, 10 and 20 sccm are referred to as ta-C, ta-CNx_{10}, and ta-CNx_{20}, respectively.

The nanotextured specimens were prepared using femtosecond laser. The prepared specimens were manufactured using an 800-nm-wavelength laser with a laser power of 1 W. The beam diameter was 4 mm and the pule length was 250 femtoseconds, resulting in a texturing pitch of approximately 770 nm, an amplitude of 260 nm, and a tip curvature of 550 nm (Figure 1a-f). In general, surface morphologies are smoother after DLC deposition due to isotropic depositing (e.g., chemical vapor deposition). On the other hand, the IBA-FAD method remains the as-deposited texturing morphology after deposition (Figure 1f). This is considered to be due to the feature of the FAD method which provides a strongly rectified straight beams, resulting in accumulation of carbon atoms from one direction.

The mold specimens were made from SKD11 (representing D2 in AISI standard) with a diameter of 16 mm and a thickness of 3 mm. Two types of SKD11 steel specimens were prepared with different surface treatment (i.e., non-hardened and hardened). We deposited the ta-C/ta-CNx coatings on the hardened SKD11 specimens.

2.2. Press Molding Test

In order to reproduce the press molding of ceramics products, we developed a compression molding device using punches, mold specimens and a die (Figure S2). Prior to press molding, we put 300 mg of ceramic particles in a space between the lower specimen and the die, and then we evenly flatten it. Subsequently, the upper mold specimen and punch were set. The clearance between the die and specimen was 50 μm for releasing compressed air during molding. During the press molding sequence, an oil compressor (BEBICON 1.5P-9.5VA6, Hitachi LTd., Japan) applied a compressive force to the upper punch for one minute. We varied the compressive pressure from 5 to 20 MPa to demonstrate the effect of compressive stress on the residual amount of ceramic particles. After the press molding, the upper mold specimen was released from the molded ceramic pellet. An electronic balance (BM-20, A&D Company, Limited, Japan) measured amount of residual particles on the mold specimen.

We used three types of ceramic particles. One was alumina (Al_2O_3) particles with an average diameter of 0.46 μm (AKP-20, Sumitomo Chemical Co., Ltd., Japan) (Figure 1g).

Alumina ceramic is widely used in industrial fields due to its characteristics (e.g., high electrical insulation, chemical inertness, hardness, and thermal resistance). Therefore, the data in the present study provides important results for the industrial use. In actual ceramic manufacturing, the particles are used as granulated particles of a few micrometers to hundreds of micrometers. However, the granulated particles usually contain chemical binders which affect the adhesion properties. Hence, we used primary particles for fundamental research on particle adhesion. Another particle was Al_2O_3 with different diameter of 2.0 μm (CB-P02, SHOWA DENKO K.K., Japan) for demonstrating the effect of particle size on the residual amount of the ceramic particles (Figure 1h). The other ceramic was silica (SiO_2) particles with an average diameter of 1.5 μm (KE-P150, NIPPON SHOKUBAI CO., LTD., Japan). The SiO_2 particles have a uniform diameter and a well-organized spherical shape (Figure 1i).

The residual mechanism of ceramic particles is elucidated using a work of adhesion per unit area. The work per unit area is a physical parameter which represents an amount of energy required to create new surfaces. The work of adhesion per unit area U is calculated using following Eq.(1) or Eq.(1)';

$$U = 2\sqrt{\gamma_1 \gamma_2} \quad (1)$$

$$U = 2\left(\sqrt{\gamma_1^h \gamma_2^h} + \sqrt{\gamma_1^d \gamma_2^d}\right) \quad (1)'$$

where γ_1 and γ_2 are surface energies of each material, and the superscripts h and d indicate the hydrogen bonding and dispersion force component, respectively. A quantitative adhesion force is also affected from the contact area between a particle and surface. Here, we introduce a work of adhesion W as following definition Eq.(2);

$$W = U \times A \quad (2)$$

where A is a contact area between a ceramic particle and surface. The contact area was measured using a nanoindenter (ENT-1100a, ELIONIX Inc., Japan) with a 900-nm-tip-radius indenter. An indentation load was 500 μN. Consequently, the area is calculated as following Eq.(3);

$$A = 2\pi R h \quad (3)$$

where R is a tip radius of the indenter and h is an indentation depth. Material and surface characteristics of the mold specimen (i.e., hardness, Young's modulus, and contact area to the indenter tip) are provide in SI-table S1. The surface energy of the particles is referred from the previous research works (SI-table S2)[113-114].

3. Result and Discussion

3.1 Effect of Compression Pressure on Residual Amount of Ceramic Particles

To demonstrate general adhesion characteristics of the ceramic particles to the mold, we conducted press molding tests at various compressive pressures using the flat non-hardened

SKD11 specimen and 0.46-μm Al_2O_3 particles. As a result, the residual amount of the particles decreases with an increase in the compressive pressure (Figure 2a). Optical images of the mold specimen surfaces also indicate that the higher compressive pressure, the less residues (Figure 2b-e).

A laser microscopy (OLS5000, Olympus Corporation, Japan) obtained the height distribution of the residues on the specimen. The results show interesting conclusions; the adhesion area decreases with an increase in the compressive pressure; the presence of residues above 3 μm in height decreases with the increase in the compressive pressure (Figure 3). The results indicate that the ceramic pellet is internally separated during the releasing sequence at lower compressive pressures, resulting in higher residue height. On the other hand, the separating position shifts outward as the molding pressure increases, resulting in the height of one or some particles.

The residual amount of ceramic particles is considered to be determined by the balance between adhesion force to the specimen and cohesive force among particles. If the cohesive force among particles is stronger than the adhesive force, the particles should be removed from the surface, and vice versa (Figure 4a,b). The density of the pellet increases under a high compressive pressure, resulting in a lower porosity.[15] The cohesive force among particles is mainly provided at the contact points.[16-19] Therefore, the decrease in the porosity leads to an increase in the cohesive force, resulting in the decrease in the residual amount shown in Figures 2.

Figure 3 shows that the height of the residues decreases with the increase in compressive pressure. Particles adhering to the mold surface have less flowability due to surface restrictions. Therefore, the decrease in porosity may begin inside of the pellet, resulting in the decrease in the residue height. Previous researches support the hypnosis because they show that inner density is higher than that of surface.[1,115] Further increase in compressive pressure causes a decrease in porosity near the surface, reducing the residual area in less than 2 μm (Figure 4c,d). Actually, SEM images of pellet surfaces show the difference in porosity due to the different compressive pressure (Figure 2f,g). The binary process for the images indicates that the surface porosity decreases from 0.53 to 0.46 as the pressure increases from 5 to 20 MPa.

In conclusion, the residues remained on the mold surface due to the strong adhesion force to the mold surface than the cohesive force among particles. When the force balance changes due to an increase in molding pressure, the residues are removed from the surface due to the stronger cohesive force among particles.

3.2 Reduction in Ceramic Residues on ta-C/ta-CNx coatings

In general, surface energy plays an important role in the adhesion of particles.[16-19] Therefore, we measured the surface energy using the sessile drop method with pure water and

diiodomethane (see Figure S3 for their appearance). The ta-C/ta-CNx coatings have lower surface energies per unit area than SKD11 specimens (Figure 5a). Among the coatings, the ta-CNx_{20} on nanotexturing shows the lowest value of 26 mJ/m^2. For ta-C/ta-CNx coatings, the surface energy decreases with the nanotexturing, whereas the surface energy increases for SKD11 specimens. The results are provided due to a feature of texturing enhancing surface characteristics. Textured surfaces have large exposed areas, resulting in the boosting effect due to the higher ratio of area to volume. In addition, texturing forms air pockets between the droplet and valley-shaped geometry. Consequently, the contact angle increases due to the presence of the air pockets. As a result, texturing changes the surface energy γ. Figure 5a shows that the hydrogen bonding component of the surface energy significantly decreases, especially non-hardened SKD11. The result is consistent with the increase in droplet contact angle from 68° to 89°. Furthermore, in the case of the SKD11 specimens, the contact angles of diiodomethane decreases, resulting in the increase in the dispersion force component. The result is considered to be obtained due to remove of surface oxide layers by the laser texturing process. Generally, the top-most surface of metal materials exists as an oxide material. The nanotexturing is created by removing the surface material using femtosecond-laser irradiation. Consequently, the removing of the oxide layer reduces electronegativity, resulting in the lower hydrogen bonding component.

We conducted the press molding tests with various flat specimens. In order to achieve the same contact pressure level for Al_2O_3 and SiO_2 particles, we selected compressive pressures of 5 MPa for 0.46-μg Al_2O_3 (Young's modulus of 390 GPa) and 20 MPa for SiO_2 (Young's modulus of 73 GPa), resulting in a Hertzian contact pressure of approximately 2.7 GPa for the non-hardened SKD11 flat specimen.

Figure 5b,c shows the relation between the residual amount of Al_2O_3 particles and the work of adhesion W. The residual amount increases with an increase in the work of adhesion between the ceramic particles and mold surface. Interestingly, the ta-C and ta-CNx coated specimens show less residues compared to non-coated specimens. In particular, the ta-C coating decreases the residual amount by 98 % due to the highest hardness. A low work of adhesion should decrease the adhesive force between the particle and mold surface. On the other hand, the cohesive force among particles does not change. Consequently, the ta-C and ta-CNx coatings, which provide a lower work of adhesion, have less residues (Figure 6). Figure 5d shows the relation between work of adhesion per unit area and residual amount. The figure clearly indicates that there is a weak relation between them. Generally, the surface energy is considered to be a dominant parameter determining adhesion characteristics. Therefore, when considering the phenomenon of adhesion, we assume perfect contact (for example, liquid to solid, or plane to plane) where the entire surface is in contact with each other. On the other hand, the present paper shows the adhesion characteristics with particles. When spherical particles come into contact, the

contact area should affect the adhesion phenomenon due to deformation under a certain load. As a result, the work of adhesion (multiplying a work of adhesion per unit area by a contact area) shows the clear relation with the adhesion amount (Figure 5b,c).

In the case of SiO_2 particles, the residual amount also increases with work of adhesion, and the increase saturates at around 1300 μg (Figure 5c). The area covered with SiO_2 residues reaches more than 94 % of the mold surface in all specimens. Therefore, the difference in residual amount should depend on the height of the residues. To clarify the mechanism of different residue heights, we measured shear adhesive forces using AFM (atomic force microscopy) (SPM-9700HT, Shimadzu corporation, Japan) in LFM (lateral force microscopy) mode.[116] As a result, the shear adhesive force increases with the work of adhesion (Figure 5e). The result indicates that the surfaces with higher works of adhesion (i.e., non-coated specimens) may strongly restrict a ceramic particle to the original position during the press molding and release processes. Figure 7 displays the adhesion mechanism of SiO_2 particles to the mold surface. When the work of adhesion is low (i.e., ta-C and ta-CNx coatings), a rearrangement of particles on the surface occurs during the release process due to the low shear adhesion force. The rearrangement increases the porosity near the surface of the pellet, resulting in less residual amount (Figure 7a). On the other hand, if the shear adhesive force is sufficiently strong, the rearrangement of the pellet surface will no longer occur. Therefore, even if the work of adhesion changed, the residual amount remained constant (Figure 7b).

3.3 Reduction in Ceramic Residues on Nanotextured Surfaces

We conducted press molding tests using nanotextured specimens. The test used SiO_2 particles which had a well-organized spherical shape. As a result, the residual amount decreases by the nanotexturing, and the ta-CNx_{20} reduces the amount by 81 %, which is the largest reduction in the present research (Figure 8a). Figure 8b shows the relation between the work of adhesion per unit area U and the residual amount. The result indicates that the residual amount increases with work of adhesion per unit area. Interestingly, the approximate straight line estimates that the residual amount starts to decrease as the work of adhesion per unit area decreases below the 72 mJ/m^2. The value is consistent with the work of adhesion per unit area between SiO_2 particles. A real surface has a distribution of surface energy due to material non-uniformity, surface roughness, and surface contamination. Therefore, the residual amount decreases with a constant slope instead of showing a sharp drop. For the flat surface, the work of adhesion has strong relation with the residual amount. Therefore, the hardest ta-C coating provides the lowest residual amount. On the other hand, the ta-CNx_{20} (the lowest surface energy) provides the lowest residual amount among nanotexturing specimens. This is due to the difference of the adhesion condition. In the case of the particle adhesion on the texturing, the adhesive force is less affected from surface hardness

due to its morphological feature. Generally, texturing increases surface area due to its three-dimensional architecture. In the case of particle contact, the textured surface increases the contact area due to the fractal effect. The JKR theory (Johnson-Kendall-Roberts theory) also indicates that total adhesive force is strongly influenced by the contacting or closing surfaces even in the absence of external loads. The theory shows that the adhesive force F is provided as follows;

$$F = -3\pi R\gamma \quad (4)$$

where R is the equivalent radius. The Eq.(4) indicates that the adhesive force is present regardless external loads. In addition, the surface profiles from AFM images reveal that there are many nano-order asperities, leading to an increase in the contact area and adhesive force. Consequently, as texturing increases the contact area, the effect of surface energy on residual amount increases. This is the mechanism that the slightly soft ta-CNx_{20} coating exhibits the lowest residual amount with nanotexturing.

The Al_2O_3 particles with a diameter of 0.46 μm drastically increases residual amount on the nanotexturing, regardless of the specimen type (Figure 9a). Here, we estimated that the size ratio of the particles to the nanotexturing could strongly affect the residual amount. Therefore, we prepared 2.0-μm Al_2O_3 particles to demonstrate the size effect. As a result, the ta-C coated nanotexturing reduces the residual amount by 84 % compared to the flat surface. For small particles (0.46-μm Al_2O_3), the particles may intrude to the texturing and be captured by the texturing protrusions (Figures 9b, 10a). On the other hand, when the particles are sufficiently large, the particles no longer intrudes to the protrusions, resulting in the decrease in the residual amount due to the lower surface energy (Figures 9a,c and 10c).

However, the nanotextured non-hardened specimen still shows an increase in residual amount of 2.0-μm Al_2O_3 due to the nanotexturing. The surface hardness and Young's modulus of non-hardened SKD11 are 4.8 GPa and 253 GPa, respectively. These values are smaller than the ta-C specimen (30 GPa in hardness and 419 GPa in Young's modulus). The calculated mean contact pressure at the tip of the nanotexturing with 2.0-μm Al_2O_3 is around 10 GPa, which is higher than the hardness of non-hardened SKD11 (4.8 GPa). Consequently, the protrusions of the non-hardened nanotexturing deform under the compressive stress, resulting in a large contact area and mechanical biting (Figure 10b).

In conclusion, the present paper provides important tips for using nanotexturing on mold surfaces. The first is the size ratio of the particles to the pitch of nanotexturing (Figure 10a). In the present research, the 0.46-μm particles strongly adhere to the 770-nm-pitch nanotexturing. However, the 1.5-μm particles show less residual amount on the nanotextured surface. Therefore, we estimate that at least the texturing size should be smaller than the particle size. Another tip is that the hardness of the texturing is important to prevent mechanical biting of particles and an increase in the contact area (Figure 10b). The other tip is that the surface energy of the coating

plays an important role in controlling particle adhesion (Figure 10c). The molding tests shows that the ta-CNx_{20}, which has a sufficient hardness of 14 GPa and a low surface energy of 26 mJ/m^2, provides an 81 % decrease in residual amount on the nanotextured surface.

4. Conclusions

In the present paper, we demonstrate the ability of ta-C/ta-CNx coatings, nanotexturing and combinations thereof to reduce ceramic-particle adhesion to the mold surface. We prepared different DLC coatings with various surface energies and hardnesses (i.e., ta-C, ta-CNx_{10}, and ta-CNx_{20}). As a result, the ta-C shows the highest hardness of 30 GPa with a surface energy of 35 mJ/m^2 on the nanotexturing. On the other hand, the nanotextured ta-CNx_{20} provides the lowest surface energy of 26 mJ/m^2. We used five types of specimens including non-hardened SKD11, hardened SKD11, and the ta-C/ta-CNx coatings for clarifying the residual mechanism.

We conducted press molding tests using the flat SKD11 specimen at various compressive pressures from 5 to 20 MPa. As a result, the residual amount of 0.46-μm Al_2O_3 decreases with the increase in the compressive pressure. In addition, residues over 3 μm in height are selectively removed as the compressive pressure increases. The result indicates that the force balance dominates the residual amount. High compressive pressure reduces porosity inside the ceramic pellet, resulting in a higher cohesive force among ceramic particles. Therefore, the particles on the top-most surface of the mold are removed along with other particles. On the other hand, if the cohesive force is not sufficiently high, the particles remains on the mold surface. In addition, the lower the compressive pressure, the thicker the highly porous layer which easily remains on the mold surface.

We conducted press molding tests with various surface coatings on the flat specimens. As a result, the residual amount decreases with a decrease in the work of adhesion. In the case of the ta-C coating for Al_2O_3 ceramic particles, the residual amount decreases by 98 % compared to non-hardened SKD11 (one of the conventional mold surfaces) due to its high hardness of 30 GPa and low surface energy per unit area of 35 mJ/m^2.

Finally, the present paper reveals effect of nanotexturing on residual amount of ceramic particles. When using SiO_2 particles with a diameter of 1.5 μm, the nanotexturing reduces the residual amount on all specimens. Especially, the ta-CNx_{20} shows the lowest residual amount of 235 μg, which is 81 % lower than that of the flat surface. On the other hand, the nanotexturing increases the residual amount of 0.46-μm Al_2O_3 particles. The result indicates that the ratio of particle size to texturing pitch is very important for reducing the residual amount. To test the hypothesis, we prepared 2.0-μm Al_2O_3 particles to demonstrate the size effect. As a result, the ta-C-coated nanotexturing reduces the residual amount by 84 % compared to the flat surface. On the other hand, the non-hardened nanotexturing specimen still shows an increase in residual amount

with the nanotexturing. Due to the lower hardness and Young's modulus of non-hardened SKD11, the contact area increases and mechanical biting occurs on the nanotexturing. In conclusion, we obtain texturing design tips; surfaces must be hard enough for compressive pressure; the texturing pitch should be shorter than the particle size; the lower the surface energy, the less residual amount.

Supporting Information

1. A schematic of coating equipment (IBA-FAD)
2. Schematic and photo images of the molding device
3. Appearance of DLC coatings
4. Mechanical and physical characteristics of the specimens and particles

Corresponding Author

*E-mail: motoyuki.murashima@mae.nagoya-u.ac.jp.

Notes

The authors declare no competing financial interest.

References

(1) Macleod, H. M. The determination of density distributions in ceramic compacts using autoradiography. Powder Technol. 1977, 16, 107-122.

(2) Aydin, İ.; Briscoe, B. J.; Şanlitürk, K. Y. The internal form of compacted ceramic components: A comparison of a finite element modelling with experiment. Powder Technol. 1996, 89, 239-254.

(3) Powell, J.; Assabumrungrat, S.; Blackburn, S. Design of ceramic paste formulations for co-extrusion. Powder Technol. 2013, 245 21-27.

(4) Muzzio, F. J.; Shinobrot, T.; Glasser, B. J. Powder technology in the pharmaceutical industry: the need to catch up fast. Powder Technol. 2002, 124, 1-7.

(5) Michrafy, A.; Ringenbacher, D.; Tchoreloff, P. Modelling the compaction behaviour of powders: application to pharmaceutical powders. Powder Technol. 2002, 127, 257-266.

(6) Werner, S. R. L.; Jones, J. R.; Paterson, A. H. J.; Archer, R. H.; Pearce, D. L. Air-suspension particle coating in the food industry: Part I - state of the art. Powder Technol. 2007, 171, 25-33.

(7) Boonyai, P.; Bhandari B.; Howes, T. Stickiness measurement techniques for food powders: a review. Powder Technol. 2004, 145, 34-46.

(8) Cuq, B.; Rondet, E.; Abecassis, J. Food powders engineering, between knowhow and science: Constraints, stakes and opportunities. Powder Technol. 2011, 208, 244-251.

(9) Turian, R. M.; Ma, T. W.; Hsu, F. L. G.; Sung, D. J. Characterization, settling, and rheology

of concentrated fine particulate mineral slurries. Powder Technol. 1997, 93, 219-233.

(10) Li, Y.; Xu, Y.; Thornton, C. A comparison of discrete element simulations and experiments for 'sandpiles' composed of spherical particles. Powder Technol. 2005, 160, 219-228.

(11) Yekeler, M.; Ulusoy, U.; Hiçyılmaz, C. Effect of particle shape and roughness of talc mineral ground by different mills on the wettability and floatability. Powder Technol. 2004, 140, 68-78.

(12) Susana, L.; Campaci, F.; Santomaso, A. C. Wettability of mineral and metallic powders: Applicability and limitations of sessile drop method and Washburn's technique. Powder Technol. 2012, 226, 68-77.

(13) Farokhipour, A.; Mansoori, Z.; Rasoulian, M. A.; Rasteh, A.; Saffar-Avval, M.; Ahmadi, G. Study of particle mass loading effects on sand erosion in a series of fittings. Powder Technol. 2020, 373, 118-141.

(14) Groenou, A. B. V. Compaction of ceramic powders. Powder Technol. 1981, 28, 221-228.

(15) Bortzmeyer, D. Modeling ceramic powder compaction. Powder Technol. 1992, 70, 131-139.

(16) Walton, O. R. Discrete characterization tools for cohesive granular material. KONA Powder Part. J. 2008, 26, 129-141.

(17) Nase, S. T., Vargas, W. L.; Abatan, A. A.; McCarthy, J. J. Discrete characterization tools for cohesive granular material. Powder Technol. 2001, 116, 214-223.

(18) Thornton, C.; Ning, Z.; A theoretical model for the stick/bounce behaviour of adhesive, elastic-plastic spheres. Powder Technol. 1998, 99, 154-162.

(19) Seville, J. P. K., Willett, C. D., Knight, P. C. Interparticle forces in fluidisation: a review. Powder Technol. 2000, 113, 261-268.

(20) Pilkington, G. A.; Harris, K.; Bergendal, E.; Reddy, A. B.; Palsson, G. K.; Vorobiev, A.; Antzutkin, O. N.; Glavatskih, S.; Rutland, M. W. Electro-responsivity of ionic liquid boundary layers in a polar solvent revealed by neutron reflectance. J. Chem. Phys. 2018, 148, 193806-1-9.

(21) Hjalmarsson, N.; Bergendal, E.; Wang, Y. L.; Munavirov, B.; Wallinder, D.; Glavatskih, S.; Aastrup, T.; Atkin, R.; Furó, I.; Rutland, M. W. Electro-Responsive Surface Composition and Kinetics of an Ionic Liquid in a Polar Oil. Langmuir 2019, 35, 15692-15700.

(22) Murashima, M.; Yoshino, S.; Kawaguchi, M.; Umehara, N. Intelligent tribological surfaces: from concept to realization using additive manufacturing. Int. J. Mech. Mater. Des. 2019, 15, 757-766.

(23) Murashima, M.; Imaizumi, Y.; Murase, R.; Umehara, N.; Tokoroyama, T.; Saito, T.; Takeshima, M. Active friction control in lubrication condition using novel metal morphing surface. Tribol. Int. 2021, 156, 106827-1-9.

(24) Taib, M. T. B.; Umehara, N.; Tokoroyama, T.; Murashima, M. The Effect of UV Irradiation to a-C:H on Friction and Wear Properties under PAO Oil Lubrication Including MoDTC and ZnDTP. Tribol. Online 2018, 13, 119-130.

(25) Murashima, M.; Oh, S. J.; Miyachi, T.; Umehara, N.; Tokoroyama, T.; Konishi, K.; Okamoto, T. Proposal of development guidline for low frictional material in oil lubrication with high permittivity material. Proc. 6th Int. Conf. Integr. Reliab. Fail. 2018, 941-942.

(26) Murashima, M.; Umehara, N.; Kousaka, Tokoroyama, T. The development of adhesion reduction method for thermoplastic CFRP and mould – the effect of mould temperature in press forming process with thermo-setting plastic-. Proc. World Tribol. Congr. 2014, 3, 2081-2083.

(27) Murashima, M.; Umehara, N.; Kousaka, H.; Deng, X. Effect of electric field on adhesion of thermoplastic resin against steel plate. Tribol. Online 2017, 12, 42-48.

(28) Barthlott, W., Neinhuis, C. Purity of the sacred lotus, or escape from contamination in biological surfaces. Planta 1997, 202, 1-8.

(29) Feng, L.; Li, S.; Li, Y.; Li, H.; Zhang, L.; Zhai, J.; Song, Y.; Liu, B.; Jiang, L.; Zhu, D. Super-hydrophobic surfaces: From natural to artificial. Adv. Mater. 2002, 14, 1857-1860.

(30) Neinhuis, C.; Barthlott, W. Characterization and distribution of water-repellent, self-cleaning plant surfaces. Ann. Bot. 1997, 79, 667-677.

(31) Quéré, D. Wetting and Roughness. Annu. Rev. Mater. Res. 2008, 38, 71-99.

(32) Roach, P.; Shirtcliffe, N. J.; Newton, M. I. Progress in superhydrophobic surface development. Soft Matter 2008, 4, 224-240.

(33) Erdemir, A. Review of engineered tribological interfaces for improved boundary lubrication. Tribol. Int. 2005, 38, 249-256.

(34) Etsion, I. Improving tribological performance of mechanical components by laser surface texturing. Tribol. Lett. 2004, 17, 733-737.

(35) Kikuchi, Y.; Ibrahim, M. D.; Ochiai, M. Evaluation of lubrication performance of foil bearings with new texturing. Tribol. Online 2019, 14, 339-344.

(36) Watanabe, K.; Seki, K.; Tadano, H.; Kaiser, F. A study on the friction reduction of seal ring for automatic transmission by applying surface texture. Tribol. Online 2017, 12, 151-154.

(37) Wang, X.; Kato, K.; Adachi, K.; Aizawa, K. Loads carrying capacity map for the surface texture design of SiC thrust bearing sliding in water. Tribol. Int. 2003, 36, 189-197.

(38) Murashima, M.; Umehara, N.; Kousaka, H. Effect of nano-texturing on adhesion of thermoplastic resin against textured steel plate. Tribol. Online 2016, 11, 159-167.

(39) Wakuda, M.; Yamauchi, Y.; Kanzaki, S.; Yasuda, Y. Effect of surface texturing on friction reduction between ceramic and steel materials under lubricated sliding contact. Wear 2003, 254, 356-363.

(40) Kovalchenko, A.; Ajayi, O.; Erdemir, A.; Fenske, G.; Etsion, I. The effect of laser surface texturing on transitions in lubrication regimes during unidirectional sliding contact. Tribol. Int. 2005, 38, 219-225.

(41) Tani, H.; Yamashita, N.; Koganezawa, S.; Tagawa, N. Taro-leaf inspired patterning of oleophobic surfaces with high wear resistance. Tribol. Online 2018, 13, 311-315.

(42) Wen, L.; Weaver, J. C.; Lauder, G. V. Biomimetic shark skin: design, fabrication and hydrodynamic function. J. Exp. Biol. 2014, 217, 1656-1666.

(43) Yonehara, M.; Okubo, H.; Tadokoro, C.; Sasaki, S.; Prakash, B. Proposal of biomimetic tribological system to control friction behavior under boundary lubrication by applying 3D metal printing process. Tribol. Online 2018, 13, 8-14.

(44) Feng, X.; Jiang, L. Design and creation of superwetting/antiwetting surfaces. Adv. Mater. 2006, 18, 3063-3078.

(45) Zhan, Y. L.; Ruan, M.; Li, W.; Li, H.; Hu, L. Y.; Ma, F. M.; Yu, Z. L.; Feng, W. Fabrication of anisotropic PTFE superhydrophobic surfaces using laser microprocessing and their self-cleaning and anti-icing behavior. Colloids Surf. A 2017, 535, 8-15.

(46) Wong, W. S. Y.; Stachurski, Z. H.; Nisbet, D. R.; Tricoli, A. Ultra-Durable and Transparent Self-Cleaning Surfaces by Large-Scale Self-Assembly of Hierarchical Interpenetrated Polymer Networks. Appl. Mater. Interfaces 2016, 8, 13615-13623.

(47) Li, S.; Page, K.; Sathasivam, S.; Heale, F.; He, G.; Lu, Y.; Lai, Y.; Chen, G.; Carmalt, C. J.; Parkin, I. P. Efficiently texturing hierarchical superhydrophobic fluoride-free translucent films by AACVD with excellent durability and self-cleaning ability. J. Mater. Chem. A 2018, 6, 17633-17641.

(48) Zhao, H.; Law, K. Y. Directional self-cleaning superoleophobic surface. Langmuir, 2012, 28, 11812-11818.

(49) Xu, Q.; Zhang, W.; Dong, C.; Sreeprasad, T. S.; Xia, Z. Biomimetic self-cleaning surfaces: synthesis, mechanism and applications. J. R. Soc. Interface 2016, 13, 20160300.

(50) Halbowax, M.; Sarnet, T.; Delaporte, Ph.; Sentis, M.; Etienne, H.; Torregrosa, F.; Vervisch, V.; Perichuaud, I.; Martinuzzi, S. Micro and nano-structuration of silicon by femtosecond laser: Application to silicon photovoltaic cells fabrication. Thin Solid Films 2008, 516, 6791-6795.

(51) Bizi-Bandoki, P.; Benayoun, S.; Valette, S.; Beaugiraud, B.; Audouard, E. Modifications of roughness and wettability properties of metals induced by femtosecond laser treatment. Appl. Surf. Sci. 2011, 257, 5213-5218.

(52) Nayak, B. K.; Iyengar, V. V.; Gupta, M. C. Efficient light trapping in silicon solar cells by ultrafast-laser-induced self-assembled micro/nano structures. Prog. Photovolt: Res. Appl. 2011, 19, 631-639.

(53) Ahmmed, K. M. T.; Grambow, C.; Kietzig, A. M. Fabrication of Micro/Nano Structures on Metals by Femtosecond Laser Micromachining. Micromachines 2014, 5, 1219-1253.
(54) Linde, D. V. D.; Sokolowski-Tinten, K.; Bialkowski, Laser-solid interaction in the femtosecond time regime. J. Appl. Surf. Sci. 1997, 109/110, 1-10.
(55) Robertson, J. Diamond-like amorphous carbon. Mater. Sci. Eng. R 2002, 37, 129-281.
(56) Vetter, 60 years of DLC coatings: Historical highlights and technical review of cathodic arc processes to synthesize various DLC types, and their evolution for industrial applications. J. Surf. Coat. Technol. 2014, 257, 213-240.
(57) Erdemir, A. Genesis of superlow friction and wear in diamondlike carbon films. Tribol. Int. 2004, 37, 1005-1012.
(58) Erdemir, A. The role of hydrogen in tribological properties of diamond-like carbon films. Surf. Coat. Technol. 2001, 146-147, 292-297.
(59) Donnet, C.; Grill, A. Friction control of diamond-like carbon coatings. Surf. Coat. Technol. 1997, 94-95, 456-462.
(60) Nishimura, H.; Umehara, N.; Kousaka, H.; Deng, X. The clarification of low friction mechanism for hydrogenated amorphous carbon by in-situ observation of frictional area. Tribol. Online 2016, 11, 341-347.
(61) Kato, K.; Umehara, N.; Adachi, K. Friction, wear and N_2-lubrication of carbon nitride coatings: a review. Wear 2003, 254, 1062-1069.
(62) Kanda, S.; Tokoroyama, T.; Umehara, N.; Fuwa, Y. In situ analysis of the tribochemical reaction of CNx by FTIR. Tribol. Online 2008, 3, 100-104.
(63) Masripan, N. A. B.; Miyahira, Y.; Nishimura, H.; Tokoroyama, T.; Umehara, N.; Fuwa, Y. Effect of transfer layer on ultra low friction of CNx under blowing dry Ar. Tribol. Online 2013, 8, 219-226.
(64) Nakao, T.; Terada, M.; Umehara, N.; Murashima. M. Noble method of surface energy estimation for local friction area with in-situ friction tester in ESEM. Proc. Asia Int. Conf. Tribol. 2018, 196-197.
(65) Nishimura, H.; Umehara, N.; Kousaka, H.; Murashima, M. Clarification of effect of transformed layer and oil film on low friction coefficient of CNx coating in PAO oil lubrication by in-situ observation of friction area with reflectance spectroscopy. Tribol. Int. 2017, 113, 383-388.
(66) Okamoto, T.; Umehara, N.; Murashima, M.; Saito, K.; Manabe, K.; Hayashi, K. The Clarification of Friction Mechanism in Oil Lubrication for CNx Coating by In-Situ Observation of Friction Area with Reflectance Spectroscopy, J. Jpn. Soc. Tribol. (in Japanese) 2018, 63, 755-767.
(67) Terada, M.; Umehara, N.; Murashima, M. The effect of atmosphere gas on surface energy

of carbonaceous hard coatings wear track by in-situ measurement in ESEM. Proc. Asia Int. Conf. Tribol. 2018 2018, 357-358.

(68) Nakao, T.; Terada, M.; Umehara, N.; Murashima, M. Effect of surface energy on friction coefficient of carbonaceous hard coatings by in-situ measurement in ESEM. Proc. 6th Int. Conf. Integr. Reliab. Fail. IRF 2018 2018, 925-926.

(69) Deng, X.; Kousaka, H.; Tokoroyama, T.; Umehara, N. Thermal stability and high-temperature tribological properties of a-C:H and Si-DLC deposited by microwave sheath voltage combination plasma. Tribol. Online 2013, 8, 257-264.

(70) Takeuchi, M.; Okuno, K.; Umehara, N.; Murashima, M. Wear properties of a-C:H and Si-DLC in pressurized high-temperature water. Proc. Asia Int. Conf. Tribol. 2018 2018, 217-218.

(71) Saito, T.; Hasebe, T.; Yohena, S.; Matsuoka, Y.; Kamijo, A.; Takahashi, K.; Suzuki, T. Antithrombogenicity of fluorinated diamond-like carbon films. Diam. Relat. Mater. 2005, 14, 1116-1119.

(72) Hasebe, T.; Shimada, A.; Suzuki, T.; Matsuoka, Y.; Saito, T.; Yohena, S.; Kamijo, A.; Shirage, N.; Higuchi, M.; Kimura, K.; Yoshimura, H.; Kuribayashi, S. Fluorinated diamond-like carbon as antithrombogenic coating for blood-contacting devices. J. Biomed. Mater. Res. A 2005, 76A, 86-94.

(73) Nemoto, K.; Umehara, N.; Tokoroyama, T.; Murashima M.; Takimoto, Y.; Nakamichi, K. Deposition of ta-C:B coating by FCVA using boron doped target and its tribological behaviors at elevated temperature up to 300°C. J. Jpn. Soc. Tribol. (in Japanese) 2018, 63, 699-705.

(74) Okamoto, T.; Umehara, N.; Murashima, M.; Saito, K.; Manabe, K.; Hayashi, K. The clarification of low friction mechanism in oil lubrication for B-DLC coating by in-situ observation of friction area. Proc. Asia Int. Conf. Tribol. 2018 2018, 319-320.

(75) Aizawa, T.; Fukuda, T. Oxygen plasma etching of diamond-like carbon coated mold-die for micro-texturing. Surf. Coat. Technol. 2013, 215, 364-368.

(76) Nakamatsu, K.; Yamada, N.; Kanda, K.; Haruyama, Y.; Matsui, S. Fluorinated diamond-like carbon coating as antisticking layer on nanoimprint mold. Jpn. J. Appl. Phys. 2006, 45, 954-956.

(77) Zhang, S.; Zeng, X.; Tang, Z.; Tan, M. J. Exploring the antisticking properties of solid lubricant thin films in transfer molding. Int. J. Mod. Phys. B 2002, 16, 1080-1085.

(78) Sasaki, T.; Koga, N.; Shirai, K.; Kobayashi, Y.; Toyoshima, A. An experimental study on ejection forces of injection molding. Precis. Eng. 2000, 24, 270-273.

(79) Bewilogua, K.; Bräuer, G.; Dietz, A.; Gäbler, J.; Goch, G.; Karpuschewski, B.; Szyszka, B. Surface technology for automotive engineering. CIRP Ann. Manuf. Technol. 2009, 58, 608-

627.

(80) Tung, S. C.; Gao, H. Tribological characteristics and surface interaction between piston ring coatings and a blend of energy-conserving oils and ethanol fuels. Wear 2003, 255, 1276-1285.

(81) Higuchi, T.; Mabuchi, Y.; Ichihara, H.; Murata, T.; Moronuki, M. Development of hydrogen-free diamond-like carbon coating for piston rings. Tribol. Online 2017, 12, 117-122.

(82) Mabuchi, Y.; Yamashita, T.; Izumi, H.; Sekikawa, T.; Nishimura, K.; Hirano, S.; Moriguchi, Y. Examination of the axial shape of the automotive valvetrain cam for engine friction reduction. Tribol. Trans. 2017, 60, 1088-1098.

(83) Kano, M. Diamond-like carbon coating applied to automotive engine components. Tribol. Online 2014, 9, 135-142.

(84) Kimock, F. M.; Knapp, B. J. Commercial applications of ion beam deposited diamond-like carbon (DLC) coatings. Surf. Coat. Technol. 1993, 56, 273-279.

(85) Casiraghi, C.; Robertson, J.; Ferrari, A. C. Diamond-like carbon for data and beer storage. Materialstoday 2007, 10, 44-53.

(86) Dearnaley, G.; Arps, J. H. Biomedical applications of diamond-like carbon (DLC) coatings: A review. Surf. Coat. Technol. 2005, 200, 2518-2524.

(87) Bhowmick, S.; Alpas, A. T. Minimum quantity lubrication drilling of aluminium– silicon alloys in water using diamond-like carbon coated drills. Int. J. Mach. Tools. Manuf. 2008, 48, 1429-1443.

(88) Ehrhardt, H. New development in the field of superhard coatings. Surf. Coat. Technol. 1995, 74-75, 29-35.

(89) Sheeja, D.; Tay, B. K.; Lau, S. P.; Shi, X.; Ding, X. Structural and tribological characterization of multilayer ta-C films prepared by filtered cathodic vacuum arc with substrate pulse biasing. Surf. Coat. Technol. 2000, 132, 228-232.

(90) Tasdemir, H. A.; Wakayama, M.; Tokoroyama, T.; Kousaka, H.; Umehara, N.; Mabuchi, Y.; Higuchi, T. Ultra-low friction of tetrahedral amorphous diamond-like carbon (ta-C DLC) under boundary lubrication in polyalpha-olefin (PAO) with additives. Tribol. Int. 2013, 65, 286-294.

(91) Tasdemir, H. A.; Wakayama, M.; Tokoroyama, T.; Kousaka, H.; Umehara, N.; Mabuchi, Y.; Higuchi, T. Wear behavior of tetrahedral amorphous diamond-like carbon (ta-C DLC) in additive containing lubricants. Wear 2013, 307, 1-9.

(92) Mahmud, K. A. H. A.; Varman, M.; Kalam, M. A.; Masjuki, H. H.; Mobarak, H. M.; Zulkifli, N. W. M. Tribological characteristics of amorphous hydrogenated (a-C:H) and tetrahedral (ta-C) diamond-like carbon coating at different test temperatures in the presence of

commercial lubricating oil. Surf. Coat. Technol. 2014, 245, 133-147.

(93) Lee, W. Y.; Umehara, N.; Tokoroyama, T.; Murashima, M.; Jang, Y. J.; Kim, J. K. Effect of substrate bias on tribological behavior of ta-C films at elevated temperatures. Proc. Sakura Symp. Mech. Sci. Eng. 2017 2017, 29-32.

(94) Liu, X.; Yamaguchi, R.; Umehara, N.; Deng, X.; Kousaka, H.; Murashima, M. Clarification of high wear resistance mechanism of ta-CNx coating under poly alpha-olefin (PAO) lubrication. Tribol. Int. 2017, 105, 193-200.

(95) Liu, X.; Yamaguchi, R.; Umehara, N.; Murashima, M.; Tokoroyama, T. Effect of oil temperature and counterpart material on the wear mechanism of ta-CNx coating under base oil lubrication. Wear 2017, 390-391, 312-321.

(96) Liu, X.; Umehara, N.; Tokoroyama, T.; Murashima, M. Effect of temperature and counterpart material on the wear behavior of ta-CNx coating in base-oil. Proc. Sakura Symp. Mech. Sci. Eng. 2017 2017, 22-25.

(97) Liu, X.; Umehara, N.; Tokoroyama, T.; Murashima, M. Tribological properties of ta-CNx coating sliding against steel and sapphire in unlubricated condition. Tribol. Int. 2019, 131, 102-111.

(98) Mabuchi, Y.; Higuchi, T.; Weihnacht, V. Effect of sp^2/sp^3 bonding ratio and nitrogen content on friction properties of hydrogen-free DLC coatings. Tribol. Int. 2013, 62, 130-140.

(99) Okamoto, T.; Umehara, N.; Tokoroyama, T.; Murashima, M. The clarification of low friction mechanism in base oil lubrication of ta-CNx coating by in-situ observation with reflectance spectroscopy. Trans. JSME (in Japanese) 2019, 85, 190-00071.

(100) Boxman, R. L.; Zhitomirsky, V.; Alterkop, B.; Gidalevich, E.; Beilis, I.; Keidar, M.; Goldsmith, S. Recent progress in filtered vacuum arc deposition. Surf. Coat. Technol. 1996, 86-87, 243-253.

(101) Shi, S.; Tay, B. K.; Tan, H. S.; Liu, E.; Shi, J.; Cheah, L. K.; Jin, X. Transport of vacuum arc plasma through an off-plane double bend filtering duct. Thin Solid Films 1999, 345, 1-6.

(102) Anders, A. Approaches to rid cathodic arc plasmas of macro- and nanoparticles: a review. Surf. Coat. Technol. 1999, 120-121, 319-330.

(103) Mabuchi, Y.; Higuchi, T.; Yoshimura, D.; Murashima, M.; Kousaka, H.; Umehara, N. Influence of carbon black in engine oil on wear of H-free diamond-like carbon coatings. Tribol. Int. 2014, 73, 138-147.

(104) Murashima, M.; Deng, X.; Izuoka, H.; Umehara, N.; Kousaka, H. Effect of oxygen on degradation of defects on ta-C coatings deposited by filtered arc deposition. Surf. Coat. Technol. 2019, 362, 200-207.

(105) Lee, W. Y.; Jang, Y. J.; Tokoroyama, T.; Murashima, M.; Umehara, N. Effect of defects on

wear behavior in ta-C coating prepared by filtered cathodic vacuum arc deposition. Diam. Relat. Mater. 2020, 105, 107789.

(106) Lee, W. Y.; Jang, Y. J.; Tokoroyama, T.; Murashima, M.; Umehara, N. Effect of defects on tribological behavior in ta-C coating deposited by Filtered Cathodic Vacuum Arc technique. Adv. Mech. Mach. Sci. 2019, 74, 3939-3944.

(107) Takikawa, H.; Izumi, K.; Miyano, R.; Sakakibara, T. DLC thin film preparation by cathodic arc deposition with a super droplet-free system. Surf. Coat. Technol. 2003, 163-164, 368-373.

(108) Mabuchi, Y.; Higuchi, T.; Inagaki, Y.; Kousaka, H.; Umehara, N. Wear analysis of hydrogen-free diamond-like carbon coatings under a lubricated condition. Wear 2013, 298-299, 48-56.

(109) Murashima, M.; Imaizumi, Y.; Umehara, N.; Tokoroyama, T. New droplet removal polishing method for diamond-like carbon with carbon fiber brush. Int. J. Autom. Technol. 2020, 14, 190-199.

(110) Miyakawa, N.; Minamisawa, S.; Takikawa, H.; Sakakibara, T. Physical–chemical hybrid deposition of DLC film on rubber by T-shape filtered-arc-deposition. Vacuum 2004, 73, 611-617.

(111) Takikawa, H.; Miyakawa, N.; Minamisawa, S.; Sakakibara, T. Fabrication of diamond-like carbon film on rubber by T-shape filtered-arc-deposition under the influence of various ambient gases. Thin Solid Films 2004, 457, 143-150.

(112) Iwasaki, Y.; Minamisawa, S.; Takikawa, H.; Sakakibara, T.; Hasegawa, H. Influence of duct bias on deposition rate of DLC film in T-shape filtered arc deposition. Vacuum 2006, 80, 1266-1271.

(113) Ramos-Tejada, M. M.; Durán, J. D. G.; Ontiveros-Ortega, A.; Espinosa-Jimenez, M.; Perea-Carpio, R.; Cibowski, E.; Investigation of alumina/(+)-catechin system properties. PartII: ζ-potential and surface free energy changes of alumina. Colloids Surf. B. Biointerface 2002, 24, 309-320.

(114) Bernard, P.; Clint, H. J. Solid wettability from surface energy components: relevance to Pickering emulations. Langmuir 2002, 18, 1270-1273.

(115) Kandeil, A.; Malherbe, M. C. D.; Critchley, S.; Dokainish, M. The use of hardness in the study of compaction behavior and die loading. Powder Technol.1977, 17, 253-257.

(116) Sümer, B.; Sitti, M. Rolling and spinning friction characterization of fine particles using lateral force microscopy based contact pushing. J. Adhes. Sci. Technol. 2008, 22, 481-506.

Figure 1. Micro/nano-geometries of specimens and particles. Texturing morphologies of (a,c,e) as-deposited and (b,d,f) DLC-coated specimens. Images are obtained using (a,b) SEM and (c,d) AFM. (e,f) Cross-section profiles of AFM images. SEM images of (g) 0.46-μm Al_2O_3, (h) 2.0-μm Al_2O_3, and (i) 1.5-μm SiO_2 particles.

Figure 2. Results of the compression molding test. (a) Relation between the residual amount and compressive pressure. Optical images of mold surfaces after the molding tests at (b) 5MPa, (c) 10 MPa, (d) 15 MPa, and (e) 20 MPa. SEM images of the compressed pellets at (f) 5 MPa and (g) 20 MPa.

Figure 3. Height distribution of residues on the mold specimens at various of compressive pressures.

Figure 4. Schematics of residual mechanism of ceramic particles on the mold surface at (a,c) low compressive and (b,d) high compressive pressure. (c,d) The height of residues depends on the compressive pressure. The arrows on a particle indicate adhesive forces of particle/particle and particle/mold.

Figure 5. (a) The surface energy per unit area of each specimen. The relation of residual amount of (b) Al_2O_3 and (c) SiO_2 particles to the work of adhesion on the flat specimens. (d) The relation of residual amount of Al_2O_3 particles to the work of adhesion per unit area. (e) Shear adhesive force measured using an AFM in LFM mode.

Figure 6. Schematics of formation of ceramic residues on a mold surface with a (a) low work of adhesion and (b) high low work of adhesion. Arrows indicate adhesive forces between a particle and a surface.

Figure 7. Schematics of formation of SiO_2 residues on a mold surface with a (a) low work of adhesion and (b) high low work of adhesion. Arrows indicate adhesive force between a particle and a surface. The purple dotted circles indicate the original position of ceramic particles before pulling and releasing.

Figure 8. (a) The residual amount of SiO_2 particles on various surfaces. (b) The relation of residual amount to work of adhesion per unit area. The orange bar indicates a work of adhesion per unit area between SiO_2 particles.

Figure 9. (a) The effect of particle size on the residual amount. SEM images of residues of (b) 0.46-μm Al_2O_3 and (c) 2.0-μm Al_2O_3 ceramic particles on nanotexturing.

Figure 10. Schematics showing the effect of the (a) texturing pitch, (b) surface hardness, and (c) surface energy on particle adhesion.

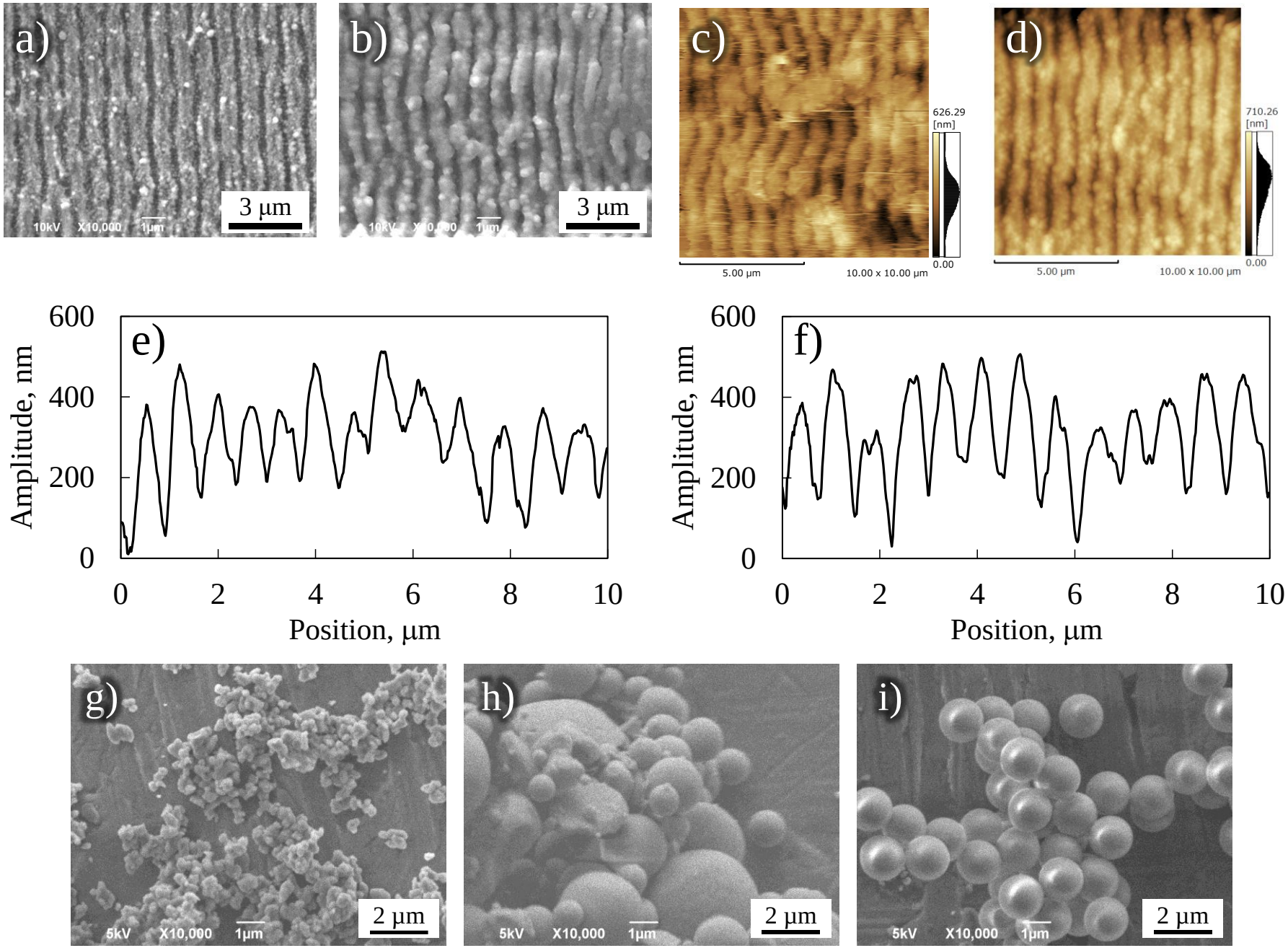
a)
3 µm
10kV X10,000 1µm
b)
3 µm
c)
626.29
[nm]
0.00
5.00 µm
10.00 x 10.00 µm
d)
710.26
[nm]
0.00
5.00 µm
10.00 x 10.00 µm
e)
Amplitude, nm
600
400
200
0
0
2
4
6
8
10
Position, µm
f)
Amplitude, nm
600
400
200
0
0
2
4
6
8
10
Position, µm
g)
2 µm
5kV X10,000 1µm
h)
2 µm
5kV X10,000 1µm
i)
2 µm
5kV X10,000 1µm

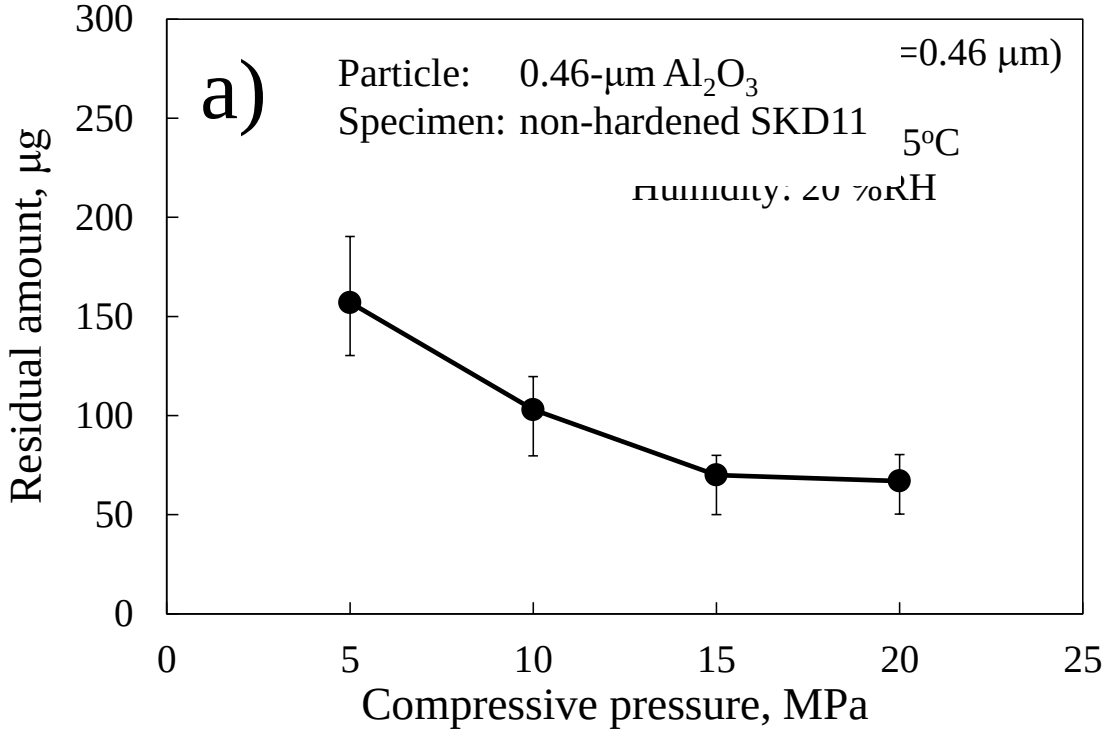
a)
Particle: 0.46-μm Al_2O_3
Specimen: non-hardened SKD11
=0.46 μm)
5°C
Humidity: 20 %RH
Residual amount, μg
300
250
200
150
100
50
0
0
5
10
15
20
25
Compressive pressure, MPa

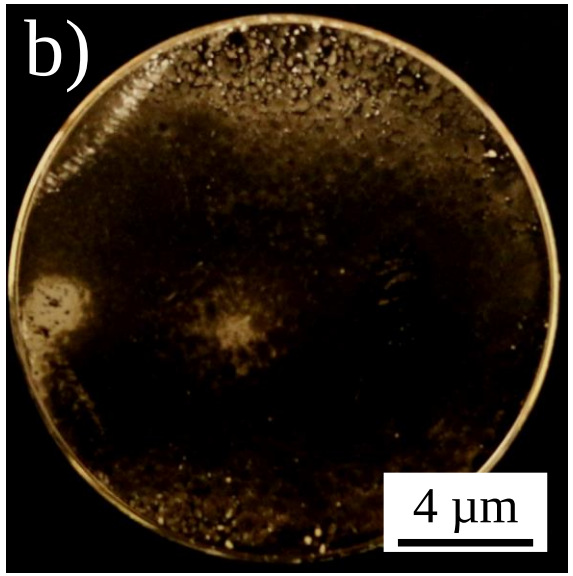
b)
4 μm

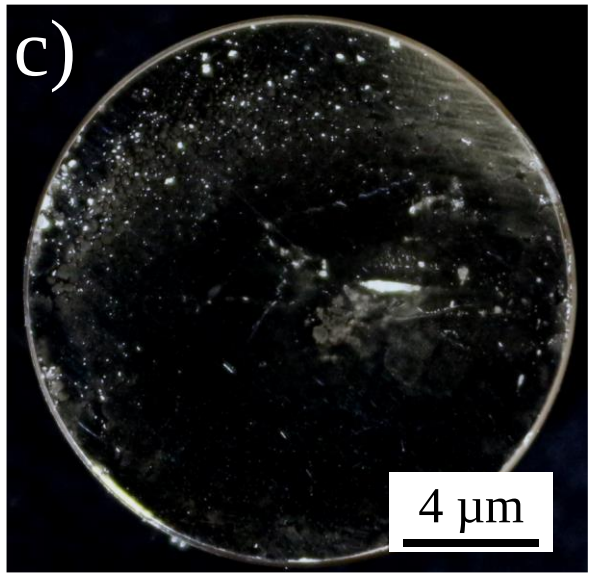
c)
4 μm

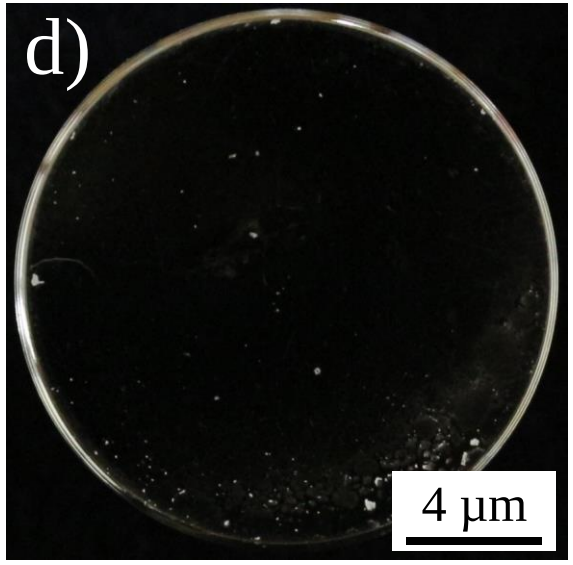
d)
4 μm

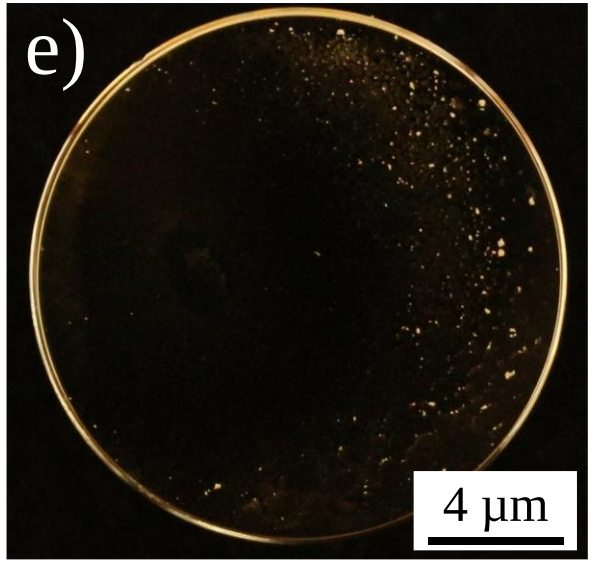
e)
4 μm

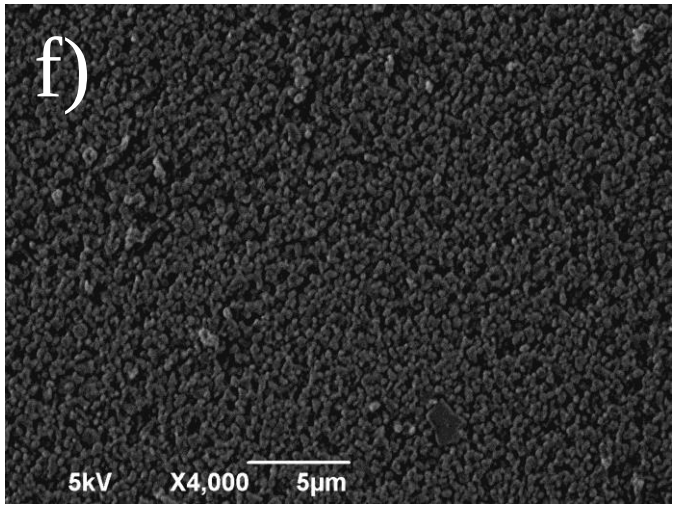
f)
5kV X4,000 5μm

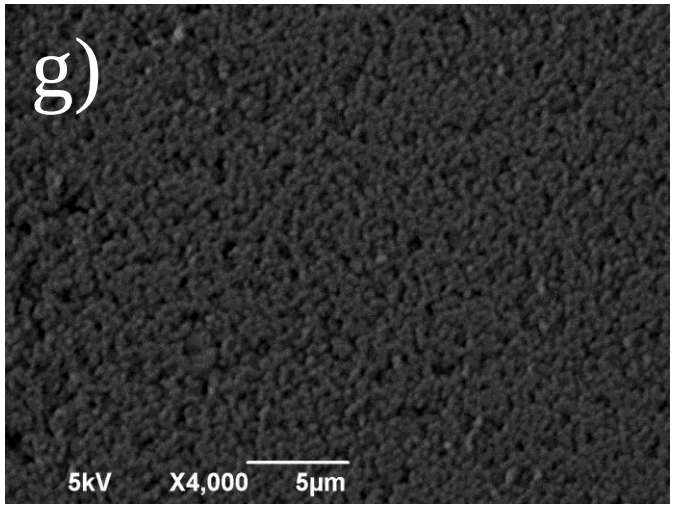
g)
5kV X4,000 5μm

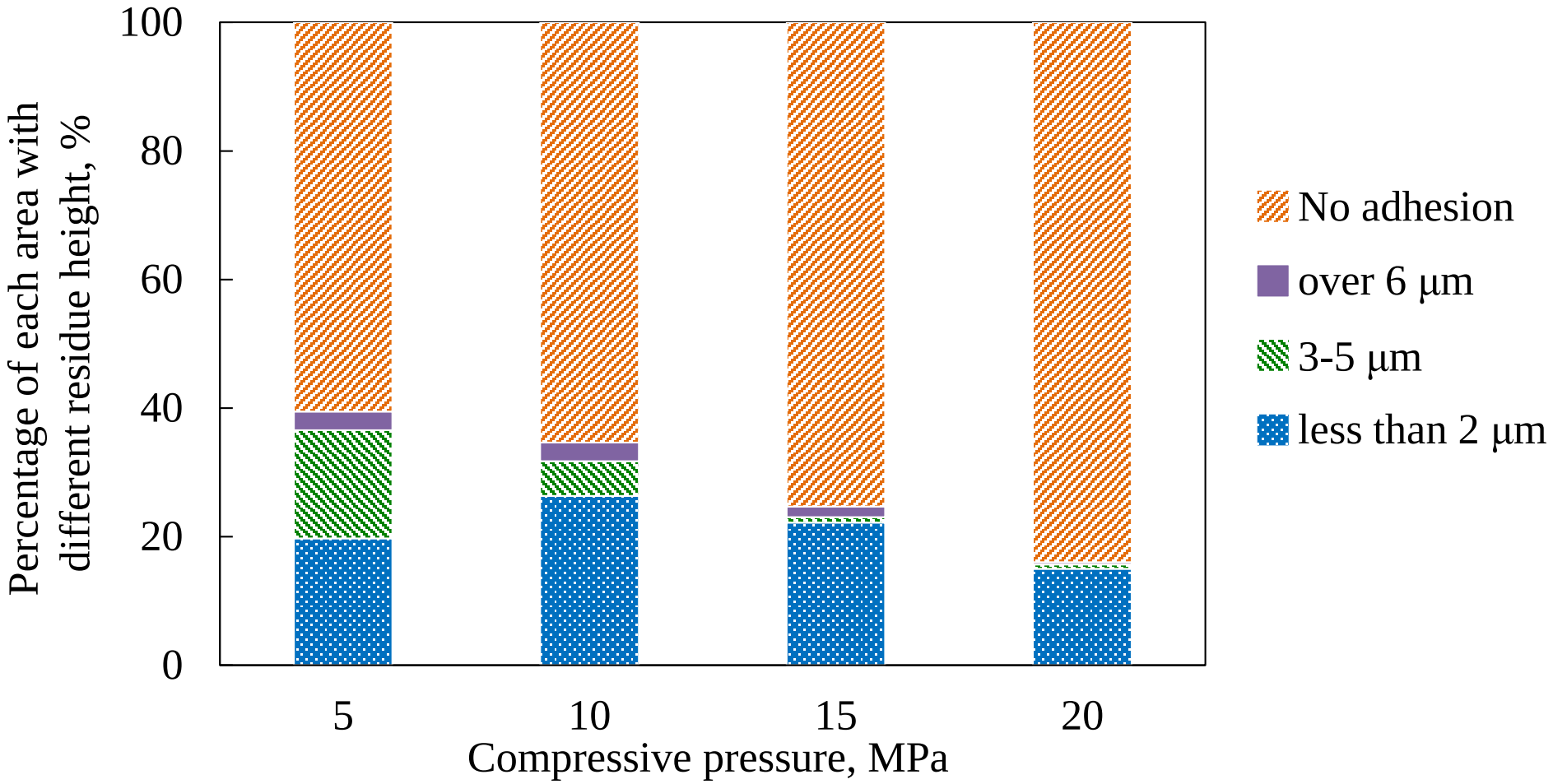
Percentage of each area with different residue height, %
100
80
60
40
20
0
5
10
15
20
Compressive pressure, MPa
No adhesion
over 6 μm
3-5 μm
less than 2 μm

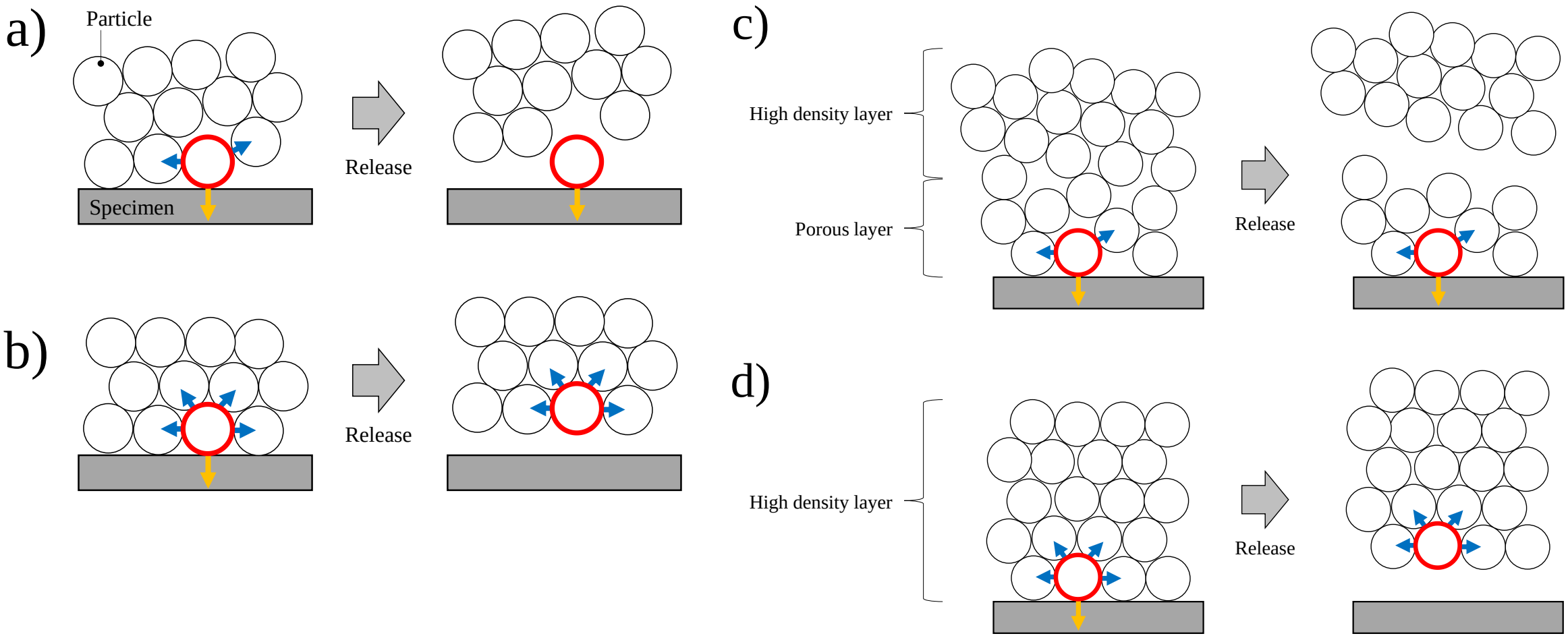
a)
Particle
Specimen
Release
b)
Release
c)
High density layer
Porous layer
Release
d)
High density layer
Release

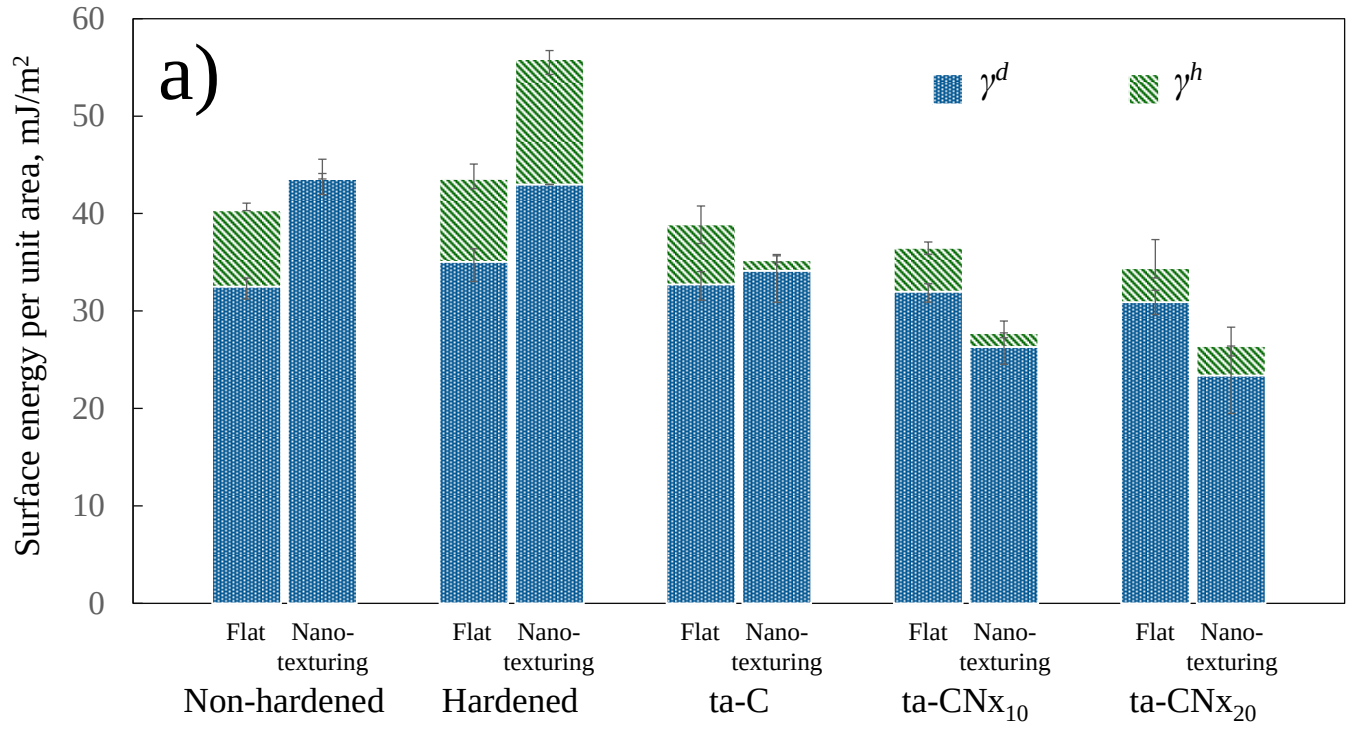
a)
Surface energy per unit area, mJ/m²
γ^d
γ^h
Flat
Nano-texturing
Non-hardened
Hardened
ta-C
ta-CNx10
ta-CNx20

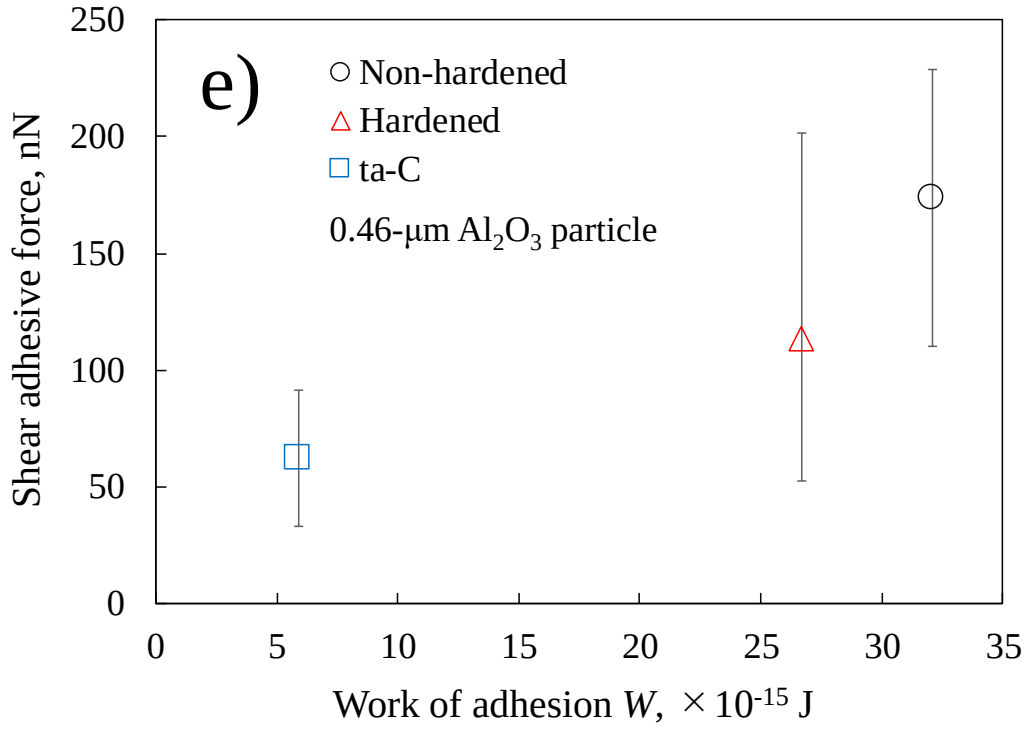
e)
Non-hardened
Hardened
ta-C
0.46-μm Al2O3 particle
Shear adhesive force, nN
Work of adhesion W, ×10-15 J

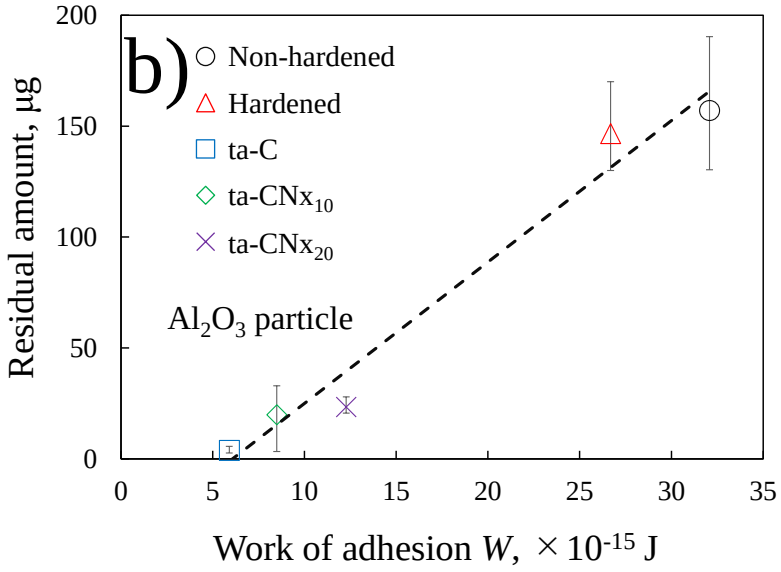
b)
Non-hardened
Hardened
ta-C
ta-CNx10
ta-CNx20
Al2O3 particle
Residual amount, μg
Work of adhesion W, ×10-15 J

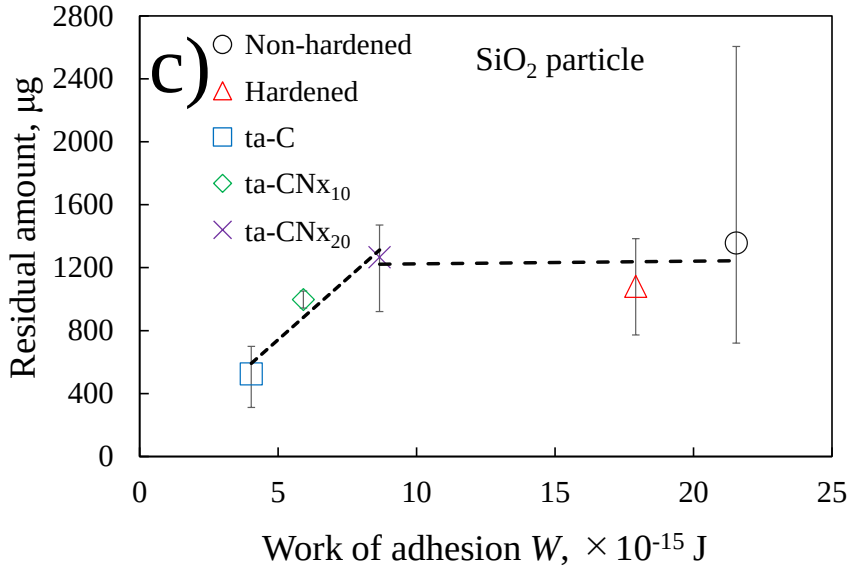
c)
Non-hardened
Hardened
ta-C
ta-CNx10
ta-CNx20
SiO2 particle
Residual amount, μg
Work of adhesion W, ×10-15 J

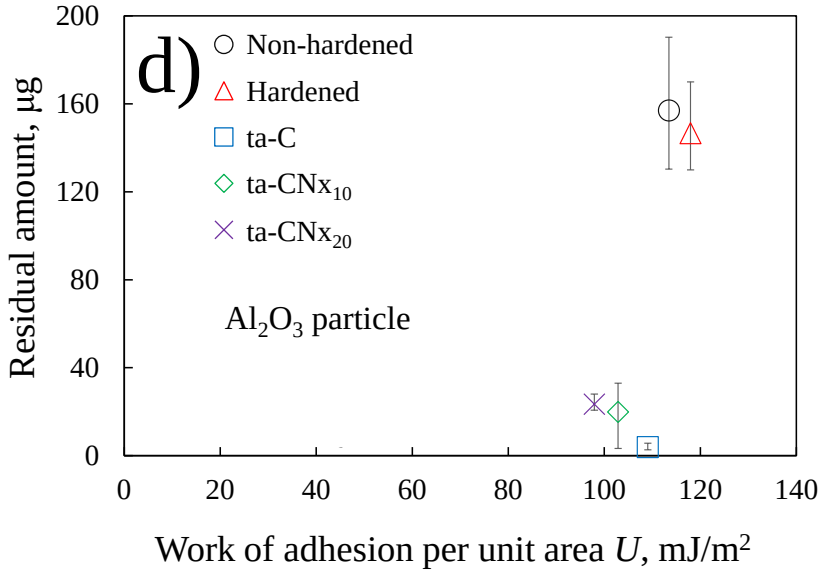
d)
Non-hardened
Hardened
ta-C
ta-CNx10
ta-CNx20
Al2O3 particle
Residual amount, μg
Work of adhesion per unit area U, mJ/m²

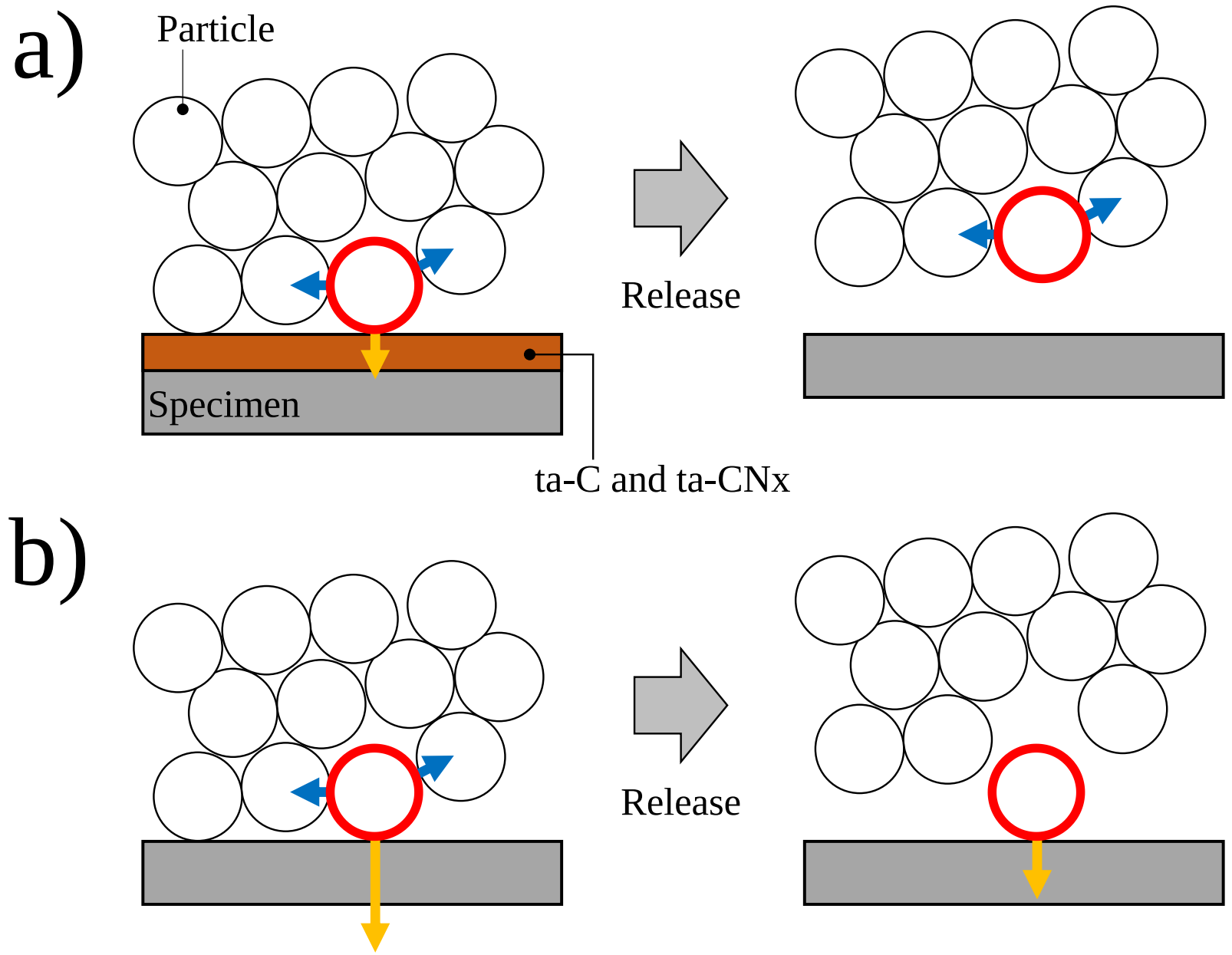
a)
Particle
Specimen
Release
ta-C and ta-CNx
b)
Release

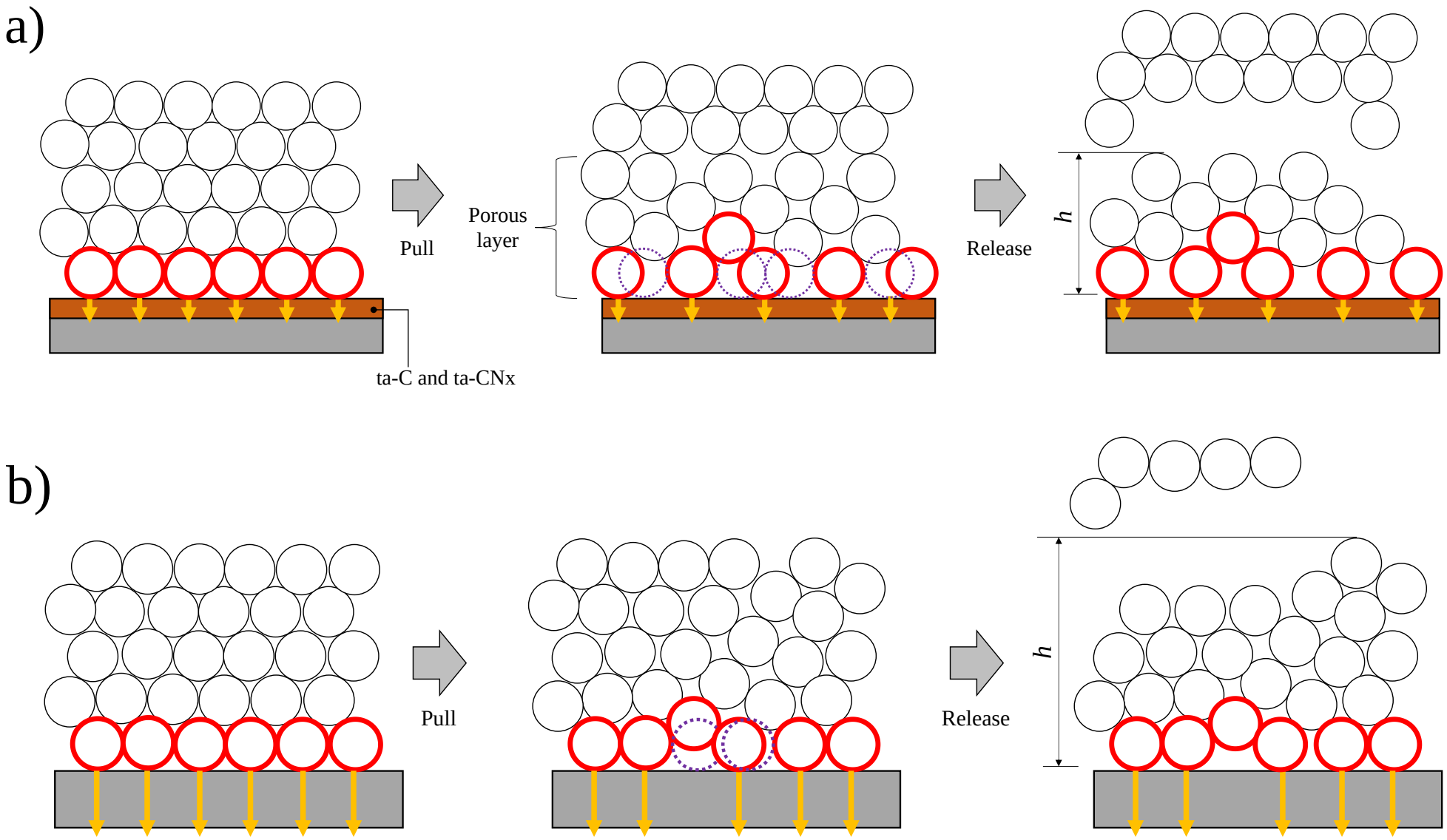
a)
Pull
Porous
layer
Release
h
ta-C and ta-CNx
b)
Pull
Release
h

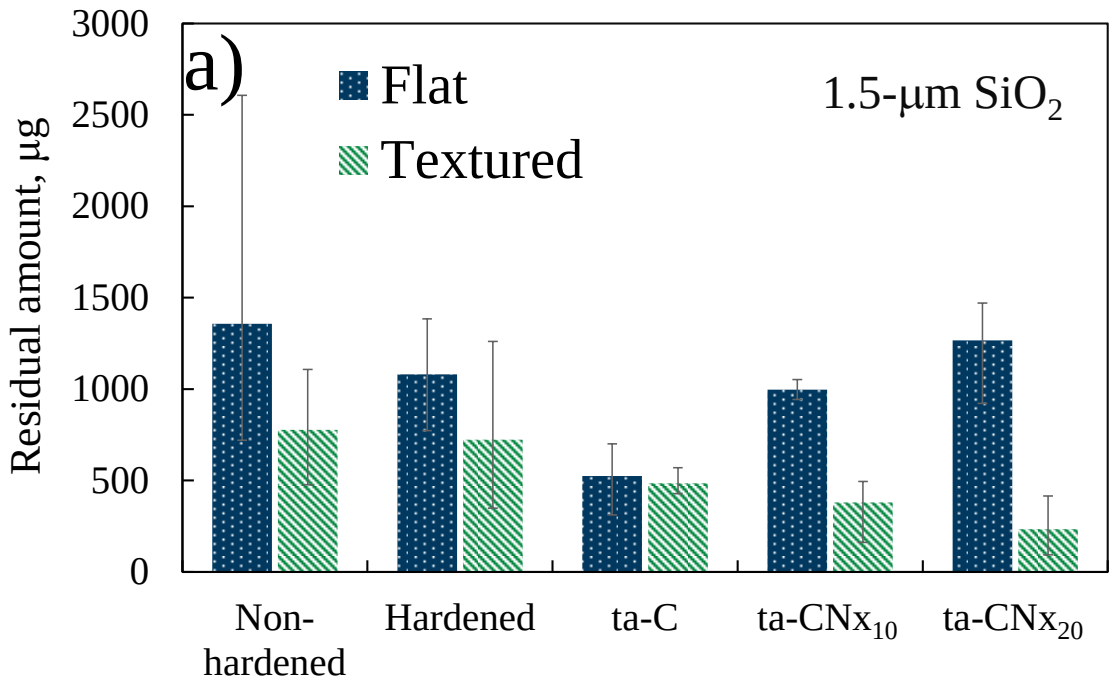
a)
Flat
Textured
1.5-μm SiO2
Residual amount, μg
3000
2500
2000
1500
1000
500
0
Non-hardened
Hardened
ta-C
ta-CNx10
ta-CNx20

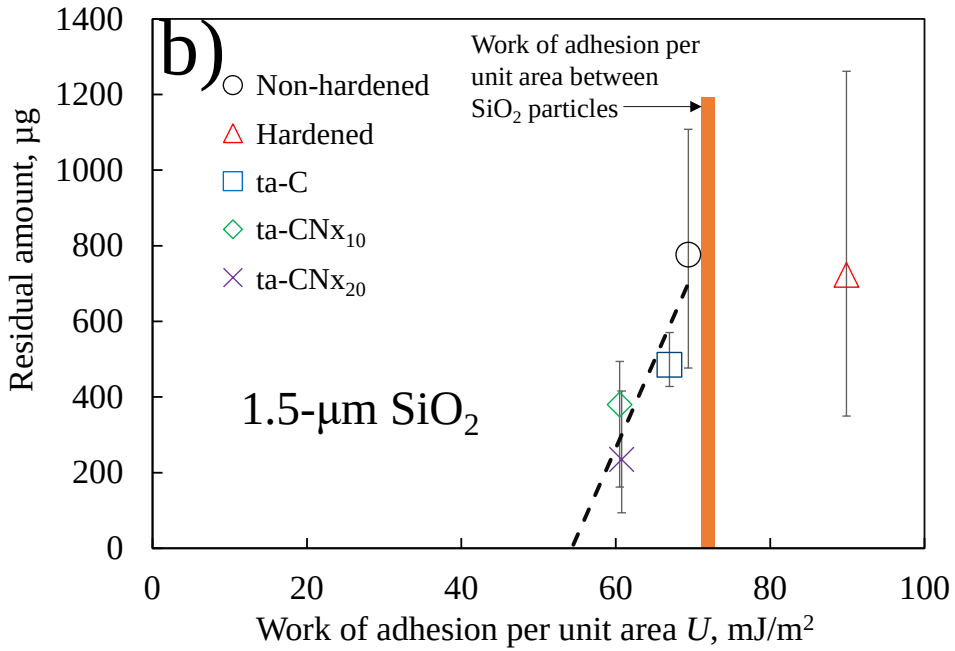
b)
Non-hardened
Hardened
ta-C
ta-CNx10
ta-CNx20
Work of adhesion per unit area between SiO2 particles
1.5-μm SiO2
Residual amount, μg
1400
1200
1000
800
600
400
200
0
0
20
40
60
80
100
Work of adhesion per unit area U, mJ/m2

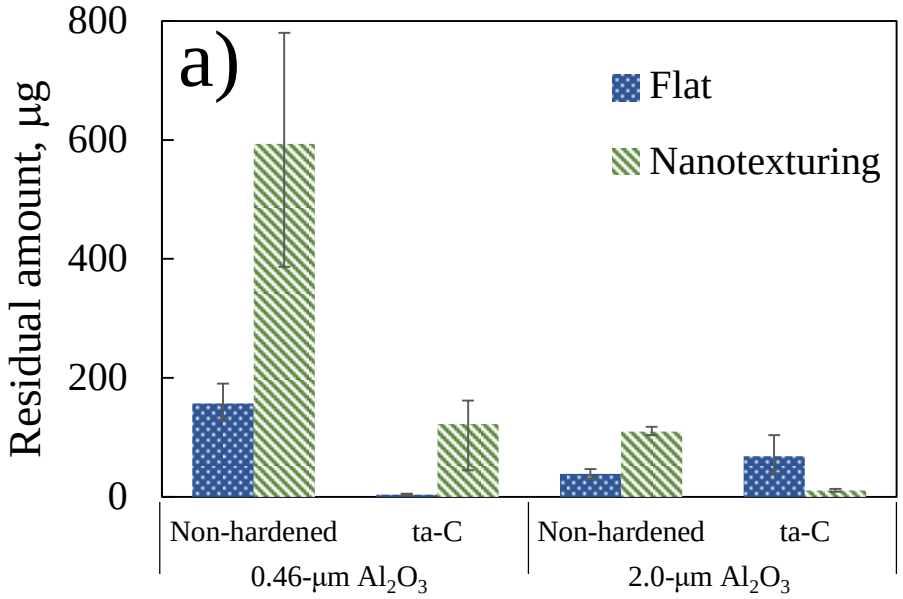
a)
Residual amount, µg
800
600
400
200
0
Flat
Nanotexturing
Non-hardened
ta-C
Non-hardened
ta-C
0.46-µm Al_2O_3
2.0-µm Al_2O_3

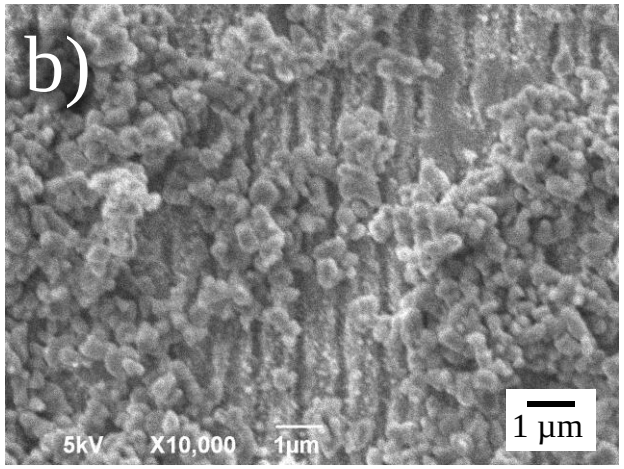
b)
5kV X10,000 1µm
1 µm

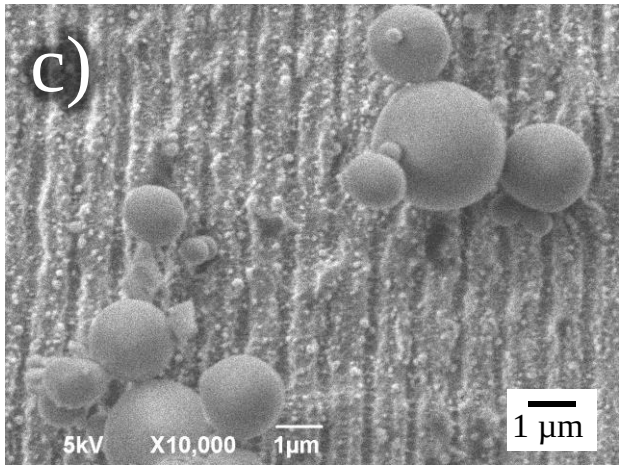
c)
5kV X10,000 1µm
1 µm

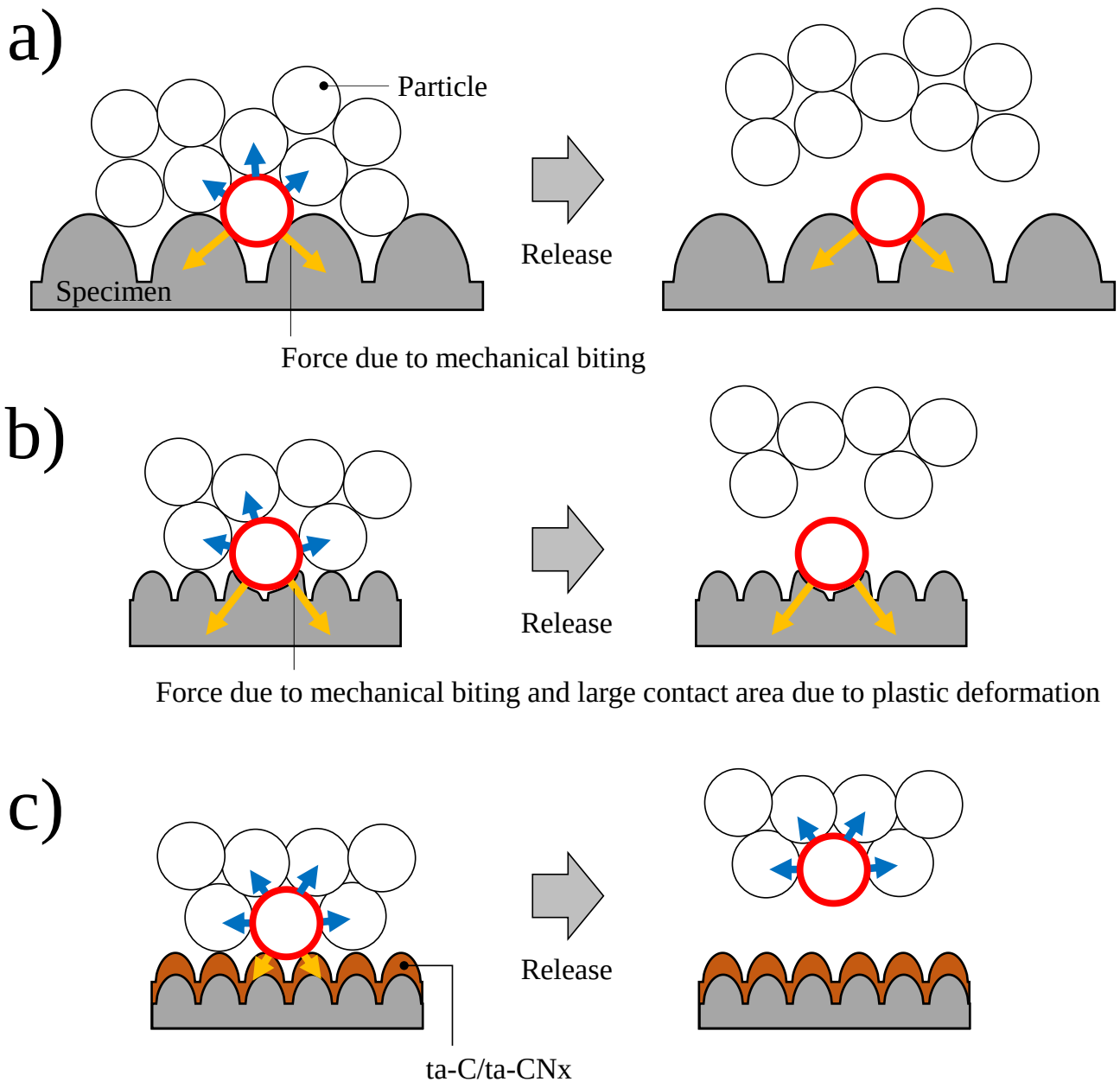
a)
Particle
Specimen
Release
Force due to mechanical biting
b)
Release
Force due to mechanical biting and large contact area due to plastic deformation
c)
Release
ta-C/ta-CNx

SUPPORTING INFORMATION

Nanotextured Mold Surface with DLC coating for Reduction in Residual Ceramic Particles

Motoyuki Murashima[1*], Koki Hojo[1], Shigehiro Ito[1], Noritsugu Umehara[1],

Takayuki Tokoroyama[1], Tomonori Takahashi[2], Minoru Imaeda[2]

[1] Department of Micro-Nano Mechanical Science and Engineering, Nagoya University
Furo-cho, Chikusa-ku, Nagoya city, Aichi 464-8603, Japan

[2] NGK Insulators, Ltd.
2-56, Suda-cho, Mizuho-ku, Nagoya city, Aichi 467-8530, Japan

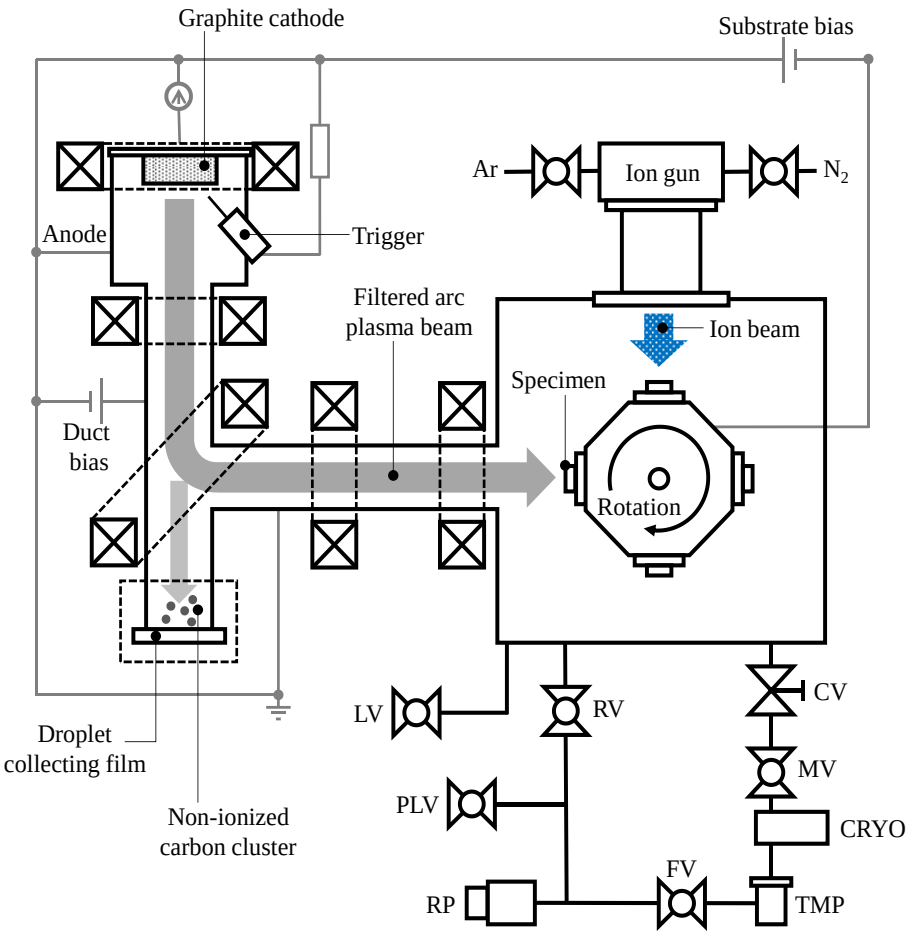

Figure S1. A schematic of IBA-FAD equipment.

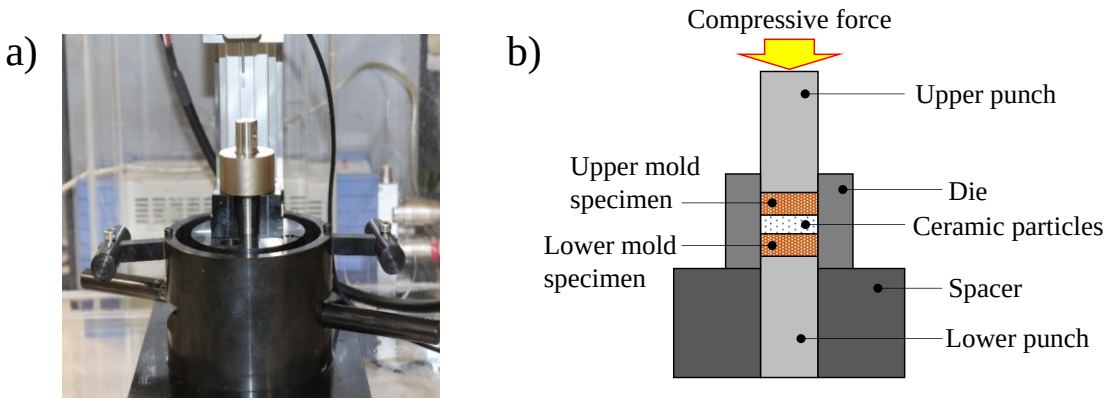

Figure S2. (a) A photo image and (b) cross-section schematic of the press molding device.

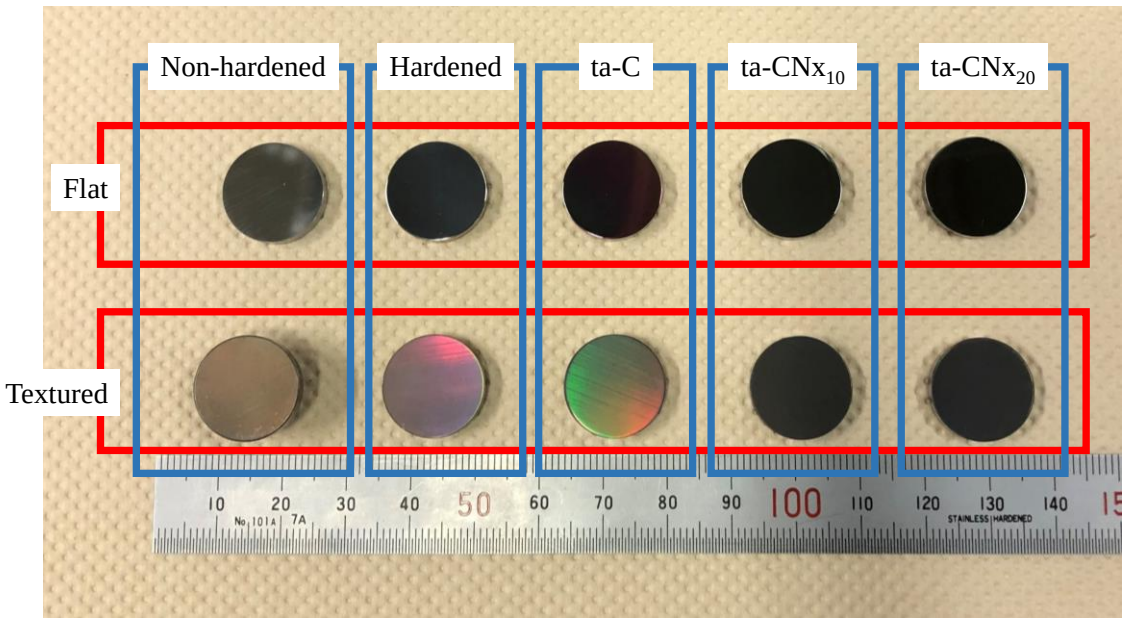

Figure S3. Appearance of DLC-coated and non-coated specimens.

Table S1. Characteristics of mold specimens with different surface treatment.
The contact area is measured using a 900-nm tip-radius indenter at 500 μN.

	Hardness, GPa	Young's modulus, GPa	Contact area to indenter tip, μm^2
non-hardened SKD11	4.8	253	0.29
hardened SKD11	8.1	255	0.23
ta-C	30	419	0.056
ta-CNx_{10}	21	331	0.085
ta-CNx_{20}	14	218	0.13

Table S2. Surface energies and its components of ceramics particles.[113-114]

	Surface eneryg γ, mJ/m^2	Surface energy of hydrogen bonding component γ^h, mJ/m^2	Surface energy of dispersion force component γ^d, mJ/m^2
Al_2O_3	94.7	40.0	54.7
SiO_2	36.2	27.0	9.2

References

(113) Ramos-Tejada, M. M.; Durán, J. D. G.; Ontiveros-Ortega, A.; Espinosa-Jimenez, M.; Perea-Carpio, R.; Cibowski, E.; Investigation of alumina/(+)-catechin system properties. PartII: ζ-potential and surface free energy changes of alumina. Colloids Surf. B. Biointerface 2002, 24, 309-320.

(114) Bernard, P.; Clint, H. J. Solid wettability from surface energy components: relevance to Pickering emulations. Langmuir 2002, 18, 1270-1273.